

Capacity-Driven Low-Interference Fast Beam Synthesis for Next Generation Base Stations

G. Oliveri,⁽¹⁾ *Senior Member, IEEE*, G. Gottardi,⁽¹⁾ *Member, IEEE*, N. Anselmi,⁽¹⁾ *Member, IEEE*, and A. Massa,⁽¹⁾⁽²⁾⁽³⁾ *Fellow, IEEE*

⁽¹⁾ *CNIT* - "University of Trento" Research Unit

Via Sommarive 9, 38123 Trento - Italy

E-mail: {giacomo.oliveri, giorgio.gottardi, nicola.anselmi, andrea.massa}@unitn.it

Website: www.eledia.org/eledia-unitn

⁽²⁾ *ELEDIA Research Center (ELEDIA@UESTC - UESTC)*

School of Electronic Engineering, Chengdu 611731 - China

E-mail: andrea.massa@uestc.edu.cn

Website: www.eledia.org/eledia-uestc

⁽³⁾ *ELEDIA Research Center (ELEDIA@TSINGHUA - Tsinghua University)*

30 Shuangqing Rd, 100084 Haidian, Beijing - China

E-mail: andrea.massa@tsinghua.edu.cn

Website: www.eledia.org/eledia-tsinghua

Capacity-Driven Low-Interference Fast Beam Synthesis for Next Generation Base Stations

G. Oliveri, G. Gottardi, N. Anselmi, and A. Massa

Abstract

The problem of the real-time multiple-input multiple-output (*MIMO*) array control when requirements on capacity performance, out-of-cell interference, and computational efficiency are simultaneously enforced is addressed by means of an innovative hybrid beamforming technique. The synthesis of the excitations of the *MIMO* system is first re-formulated as that of matching an ideal “hybrid” pattern fitting *capacity* or *low-interference* constraints along the angular coordinates. Then, a non-iterative processing scheme is derived for each *MIMO* beam where numerically-efficient synthesis techniques are profitably combined. Representative results, from an extensive numerical validation, are discussed to show, also comparatively, the advantages and the current limitations of the proposed synthesis method when dealing with different propagation scenarios, number of transmitters/receivers, and noise levels.

Key words: Phased arrays; MIMO Base Stations; 5G Communications; Beampattern Synthesis; Zero-Forcing Processing.

1 Introduction and Rationale

Multiple-Input Multiple-Output (*MIMO*)-based antenna arrays are expected to be a key component of future base stations (*BSs*) for 5G communications systems and beyond in order to meet increasingly challenging requirements in terms of data rate and reconfigurability [1]-[6]. The emergence of *MIMO* processing in antenna arrays will have a significant impact on the conception and the implementation of the design procedures for *BSs* and their real-time control [2][6]. As a matter of fact, most beamforming methods and array synthesis techniques have been traditionally conceived for the optimization of free-space properties [7][8] such as gain, sidelobe profile, power-transfer-efficiency [9][10], and null positions, but there are other performance indexes to be assessed when *MIMO* processing is at hand [2][6]. Thus, an exhaustive revision of traditional array design techniques as well as beamforming strategies is necessary to meet the needs and the performance targets of next-generation *BSs* [2][6]. In such a framework, innovative paradigms for capacity-oriented array synthesis have been recently introduced [6]. By recasting the design problem to the maximization of the link quality (i.e., the sum-rate capacity as a function of the *BS* array, the user terminal antenna features/locations, and the propagation environment), a significant improvement of the communication performance with respect to traditional array designs has been yielded [6]. As a by-product, it has been also proved that the patterns synthesized with usually-adopted methods (e.g., the popular zero forcing [*ZF*] technique [11][12]) generally do not focus the power towards the receiver direction as in traditional beamforming methods (e.g., Taylor, Dolph, Slepian synthesis techniques [7][8]), but they rather exhibit “distorted” and multi-lobes shapes [6] even when regular fully-populated architectures are used. This implies that there is a fundamental challenge, from both the theoretical and the practical viewpoint, to be addressed in future *BSs* for mobile cellular communications when profitably exploiting purely capacity-driven beamforming methods. Indeed, an excellent information transfer rate can be obtained at the expenses of a not *a-priori* controllable spatial distribution of the radiated power [6] that may result in unacceptable sidelobes and, consequently, critical out-of-sector interferences.

In principle, traditional beamforming techniques (e.g., the methods based on convex programming and/or evolutionary optimization strategies [13]-[17]) could be adapted to jointly handle

capacity-driven and out-of-cell interference requirements in *MIMO* BSs. However, realistic massive *MIMO* scenarios require the synthesis and the real-time update of a large number of beams with minimum efforts and maximum scalability. Consequently, applying a local/global iterative optimization scheme for each beam at every update step may be impractical and/or unfeasible due to the associated computational costs [15][18].

In this paper, an innovative scalable hybrid array synthesis method is proposed, as a complement to existing techniques, to simultaneously yield (i) capacity-oriented radiation performance and (ii) out-of-cell sidelobe control, while also featuring (iii) a low-cost processing. To address these contrasting objectives, the integration of a capacity-driven weighting scheme and a low-sidelobe constrained synthesis is proposed. More specifically, a computationally-efficient non-iterative hybrid capacity/sidelobe-driven (“*HCS*”) approach is derived where, for each beam, (*Step 1*) two auxiliary sets of excitations and the associated patterns are firstly synthesized according to the capacity-maximization strategy [6] (“*Max C*” strategy) and an interference-controlled technique denoted as “*Low I*” method. Then (*Step 2*), an ideal *hybridized pattern* is defined by setting to the “*Max C*” pattern and to the “*Low I*” pattern the in-sector and the out-of-sector angular portions of the radiated power, respectively. Finally (*Step 3*), the array excitations are determined to radiate the best angular approximation of the ideal *hybridized pattern*.

It is worthwhile to notice that such an approach could be potentially sub-optimal owing to the fact that no global optimization is carried out despite the nonlinearity of the problem, but it is a suitable and profitable solution for real systems and applications. Indeed, the paradigm behind the *HCS* method is motivated by the following theoretical and practical argumentations: (i) widely-adopted capacity-driven beamforming techniques (e.g., the *ZF* scheme [6][11][12]) do not easily integrate sidelobe constraints to control inter-cell interferences; (ii) the iterative local/global optimization of the capacity performance and of the sidelobe profiles for each beam, even though ideally viable, may be practically unfeasible due to the computational costs and the convergence issues when dealing with real-time massive *MIMO* operations; (iii) a suitable trade-off between capacity maximization, sidelobe control, and computational efficiency is mandatory to derive a beamforming scheme of practical interest; (v) several non-iterative array design techniques are available in the state-of-the-art literature to match the samples of a reference ideal

pattern [8] and they can be effectively customized to address the *hybridized pattern* synthesis of the *Step 3* of the *HCS*. Finally, *(iv)* the *HCS* paradigm is fully general, so it can be seamlessly customized to accommodate more/less computationally-demanding and performing techniques to solve each step of its implementation according to the available computational power, real-time needs, and expected link quality performance.

To the best of the authors' knowledge, the main innovative contributions of this research work are *(i)* the introduction of a computationally-efficient excitation synthesis method to jointly address the maximization of the capacity and the control of the sidelobes; *(ii)* the derivation of a real-time beamforming procedure easily extendable to account for additional features beyond inter-cell interference minimization in massive *MIMO* processing scenarios (e.g., static/dynamic jamming rejection, null positioning); *(iii)* the numerical assessment of the proposed approach in terms of link quality, rejection of out-of-sector interferences, and computational complexity in comparison with widely-adopted capacity-driven and sidelobe-minimizing methods, as well.

The outline of the paper is as follows. First, the beamforming problem is formulated (Sect. 2), then the hybrid synthesis technique is illustrated (Sect. 3). A selected set of numerical examples, drawn from an extensive validation study, is presented and discussed to give some insights to the interested readers of the features and the potentialities of the proposed approach also in comparison with both state-of-the-art traditional and capacity-oriented techniques (Sect. 4). Some conclusions are finally drawn (Sect. 5).

2 Problem Statement and Mathematical Formulation

With reference to the benchmark scenario in Fig. 1, let us consider a transmitting linear array that operates as a *BS* antenna in a multi-user multi-antenna downlink communication mode⁽¹⁾. Under the assumptions of *(i)* single-carrier band-pass digitally-modulated signals at the transmitters observed for the duration of a single pulse⁽²⁾, *(ii)* equal power distribution among the

⁽¹⁾Such a benchmark architecture has been chosen according to its relevance for 5G *BSs*. However, the same paradigm can be generalized to any arbitrary architecture.

⁽²⁾The multi-carrier multi-pulse cases can be seamlessly derived by taking into account the carrier/pulse indexes in each quantity within the mathematical formulation.

downlink beams, and (iii) mutual incoherence among the signal and the noise for each beam, the average *MIMO* downlink sum-rate capacity \mathcal{C}_{ave} of the *BS* across P propagation scenarios turns out to be [6]

$$\mathcal{C}_{ave} \triangleq \frac{1}{P} \sum_{p=1}^P \mathcal{C}^{(p)} \quad (1)$$

where $\mathcal{C}^{(p)}$ is the capacity of the p -th ($p = 1, \dots, P$) propagation scenario at the carrier frequency f given by

$$\mathcal{C}^{(p)} \triangleq \sum_{\chi=V,H} \sum_{r=1}^R \mathcal{C}_{\chi,r}^{(p)} \quad (2)$$

$\mathcal{C}_{\chi,r}^{(p)}$ being the downlink capacity of the χ -th ($\chi \in \{V, H\}$) polarization at the r -th ($r = 1, \dots, R$) receiving antenna equal to [6][12]

$$\mathcal{C}_{\chi,r}^{(p)} \triangleq \log_2 \left(1 + \frac{\left| \left[\mathbf{g}_{\chi,r}^{(p)} \right]' \mathbf{w}_{\chi,r}^{(p)} \right|^2}{\mu_{\chi,r}^{(p)} + \frac{2R\sigma^2(f)}{\Omega}} \right) \quad (3)$$

where $\sigma^2(f)$ is the noise power, which is assumed constant across all the receivers for the sake of simplicity, Ω is the total power radiated by the *BS*, \cdot' stands for the transpose operator, and

$$\mu_{\chi,r}^{(p)} \triangleq \left\{ \sum_{\psi=V,H} \sum_{q=1}^R \left| \left[\mathbf{g}_{\psi,q}^{(p)} \right]' \mathbf{w}_{\psi,q}^{(p)} \right|^2 \right\} - \left| \left(\mathbf{g}_{\chi,r}^{(p)} \right)^T \mathbf{w}_{\chi,r}^{(p)} \right|^2 \quad (4)$$

is the *intra-cell multi-user interference* at the r -th ($r = 1, \dots, R$) receiving antenna on the χ ($\chi \in \{V, H\}$) polarization. Moreover, $\mathbf{g}_{\chi,r}^{(p)} \triangleq \left\{ g_{\chi,\psi}^{(p)} \left(\underline{\rho}_t, \underline{\rho}_r \right); t = 1, \dots, T; \psi \in \{V, H\} \right\}$ ($\chi \in \{V, H\}; r = 1, \dots, R$) is a frequency-domain complex vector whose (t, ψ) -th entry, $g_{\chi,\psi}^{(p)} \left(\underline{\rho}_t, \underline{\rho}_r \right)$, is the Fourier transform at the frequency f of the time-domain Green's function modeling the electromagnetic propagation between the ψ -polarization ($\psi \in \{V, H\}$) of the t -th ($t = 1, \dots, T$) transmitting antenna and the χ -polarization ($\chi \in \{V, H\}$) of the r -th ($r = 1, \dots, R$) receiving element in correspondence with the p -th ($p = 1, \dots, P$) scenario, $\underline{\rho}_t = (x_t, y_t, z_t)$ and $\underline{\rho}_r = (x_r, y_r, z_r)$ being the location of the t -th ($t = 1, \dots, T$) transmitting and the r -th ($r = 1, \dots, R$) receiving antennas, respectively, while $\mathbf{w}_{\chi,r}^{(p)} \triangleq \{w_{\chi,\psi,r,t}^{(p)}; t = 1, \dots, T; \psi \in \{V, H\}\}$ ($\chi \in \{V, H\}; r = 1, \dots, R$) is the excitation vector affording the (χ, r) -beam

(i.e., the pattern responsible for the transfer of information towards the χ -polarization of the r -th receiving antenna), whose (t, ψ) -th entry, $w_{\chi, \psi, r, t}^{(p)}$, is the Fourier transform of the linear excitation as applied to the ψ -polarization ($\psi \in \{V, H\}$) of the t -th ($t = 1, \dots, T$) transmitting antenna to synthesize the (χ, r) -beam ($\chi \in \{V, H\}$; $r = 1, \dots, R$) at the frequency f in the p -th ($p = 1, \dots, P$) scenario.

It is worth remarking that (1)-(4) hold true regardless of the array architecture (e.g., regular, thinned, sparse, clustered, overlapped) adopted in the *BS* [13][6]. On the other hand, while (1) quantifies the “quality” of the connections between the *BS* and the terminals within the cell of coverage [12][6], it does not take into account the out-of-sector interferences, these latter being a key issue in multi-cell scenarios. To give a more reliable/complete figure of merit for the *BS* performance, the term (4) may be generalized to account for the presence and the locations of the users in the nearby cells, for instance, by extending the summation also to the out-of-sector receivers. Unfortunately, the real-time evaluation of such an index, which is needed for the pattern synthesis, would require the *BS* to continuously sense the channel to update the Green’s frequency-domain complex vector for all the out-of-cell users, as well. This would considerably convolute the already demanding massive *MIMO* channel estimation process. Alternatively, the out-of-sector total interference \mathcal{I}_{ave} can be computed as the average of all the out-of-cell interferences across the P propagation scenarios

$$\mathcal{I}_{ave} \triangleq \frac{1}{P} \sum_{p=1}^P \mathcal{I}^{(p)}, \quad (5)$$

the p -th ($p = 1, \dots, P$) contribution, $\mathcal{I}^{(p)}$, being efficiently estimated as the normalized integral of the pattern sidelobes outside the cell sector. More specifically,

$$\mathcal{I}^{(p)} \triangleq \sum_{\chi=V,H} \sum_{r=1}^R \mathcal{I}_{\chi,r}^{(p)} \quad (6)$$

where $\mathcal{I}_{\chi,r}^{(p)} \triangleq \frac{\int \int_{\{\theta, \varphi\} \notin \Xi} |A_{\chi,r}^{(p)}(\theta, \varphi)|^2 d\theta d\varphi}{\int \int_{\{\theta, \varphi\}} |A_{\chi,r}^{(p)}(\theta, \varphi)|^2 d\theta d\varphi}$ is the out-of-sector interference ratio of the (χ, r) -beam ($\chi \in \{V, H\}$; $r = 1, \dots, R$) at the frequency f in the p -th ($p = 1, \dots, P$) scenario, $\Xi \triangleq \{\theta_{\min} \leq \theta \leq \theta_{\max}; \varphi_{\min} \leq \varphi \leq \varphi_{\max}\}$ is the angular sector defining the coverage cell, and $A_{\chi,r}^{(p)}(\theta, \varphi)$

is the the far-field pattern of the (χ, r) -beam ($\chi \in \{V, H\}$; $r = 1, \dots, R$) at the frequency f in the p -th ($p = 1, \dots, P$) scenario given by

$$A_{\chi,r}^{(p)}(\theta, \varphi) = \mathcal{F}[\mathbf{w}_{\chi,r}^{(p)}] \triangleq \sum_{\psi=V,H} \sum_{t=1}^T \left(w_{\chi,\psi,r,t}^{(p)} \times E_{\psi,t}(\theta, \varphi) \exp \left[j \frac{2\pi f}{c_0} (\underline{\rho}_t \cdot \hat{\underline{\rho}}) \right] \right) \quad (7)$$

c_0 being the speed of light. Moreover, $E_{\psi,t}(\theta, \varphi)$ is the embedded element factor of the ψ -polarization ($\psi \in \{V, H\}$) of the t -th ($t = 1, \dots, T$) transmitting antenna, $\hat{\underline{\rho}} \triangleq (\sin \theta \cos \varphi, \sin \theta \sin \varphi, \cos \theta)$ is the unit vector in spherical coordinates, while $\mathcal{F}[\cdot]$ stands for the pattern/excitation transformation operator.

Accordingly the *Capacity-driven and Out-of-sector Interference Mitigation (COIM)* synthesis problem can be stated as that of “computing the BS array excitations, $\mathbf{w}_{\chi,r}^{(p)}$ ($\chi \in \{V, H\}$; $r = 1, \dots, R$; $p = 1, \dots, P$) so that (i) the average MIMO downlink sum-rate capacity, \mathcal{C}_{ave} , is maximized and (ii) the out-of-sector total interference, \mathcal{I}_{ave} , is mitigated across all P propagation scenarios.”

3 HCS Array Synthesis Method

To address the *COIM* synthesis problem stated in Sect. 2, traditional excitation design methods (e.g., Taylor, Dolph, Slepian techniques [7][8]) are not suitable since they are formulated to fit free-space performance requirements (e.g., gain, mainlobe width/shape, null positions, sidelobe level, etc ...) [7][8]. Otherwise, synthesis techniques devoted to the maximization of the average MIMO downlink sum-rate capacity [e.g., dirty-paper coding (*DPC*)] do not control the out-of-sector total interference [6][12][11]. The same holds true for sub-optimal capacity-oriented techniques based on *ZF*, which are widely employed because of the superior numerical efficiency and the easier implementation with respect to *DPC* [6]. In principle, an alternative solution might be that of recasting the synthesis problem at hand to an optimization one by first defining a single/multi-objective cost function, which depends on \mathcal{C}_{ave} and \mathcal{I}_{ave} , then adopting a suitable global optimization strategy possibly featuring an evolutionary approach [15][16][19]. However, this is not viable in realistic massive MIMO scenarios because of the infeasibility/costs of several (i.e., one per each (χ, r) -beam and per time-instant) iterative op-

timizations to adjust/modify the *MIMO* patterns in real time according to the user movements and the scenario variability.

In this paper, the *COIM* array design is formulated as a piecewise pattern matching problem for every p -th ($p = 1, \dots, P$) propagation scenario where the *BS* excitations are set to approximate the maximum-capacity pattern [i.e., $A_{\chi,r}^{(p)}(\theta, \varphi) \approx A_{\chi,r}^{(p),C}(\theta, \varphi)$] and the low-sidelobe pattern [$A_{\chi,r}^{(p)}(\theta, \varphi) \approx A_{\chi,r}^{(p),\mathcal{I}}(\theta, \varphi)$] in the in-sector ($\{\theta, \varphi\} \in \Xi$) and in the out-of-cell ($\{\theta, \varphi\} \notin \Xi$) portion of each received (χ, r) -beam ($\chi \in \{V, H\}$; $r = 1, \dots, R$), respectively. Accordingly, the arising *HCS* synthesis method is then implemented as a three-step process where, for each (χ, r) -beam ($\chi \in \{V, H\}$, $r = 1, \dots, R$) and p -th scenario ($p = 1, \dots, P$), (Step 1 - *Auxiliary Pattern Setup*) the auxiliary/reference patterns $A_{\chi,r}^{(p),C}(\theta, \varphi)$ and $A_{\chi,r}^{(p),\mathcal{I}}(\theta, \varphi)$ are first synthesized, then (Step 2 - *Hybrid Pattern Definition*) they are combined into a piece-wise hybridized one $\tilde{A}_{\chi,r}^{(p)}(\theta, \varphi)$, and finally (Step 3 - *Trade-Off Excitation Synthesis*) the tradeoff excitations $\mathbf{w}_{\chi,r}^{(p)}$ are computed so that the radiated pattern $A_{\chi,r}^{(p)}(\theta, \varphi)$ satisfies the matching condition $A_{\chi,r}^{(p)}(\theta, \varphi) \approx \tilde{A}_{\chi,r}^{(p)}(\theta, \varphi)$.

As for the “*Auxiliary Pattern Setup*” (Step 1) and the synthesis of the reference maximum-capacity pattern, $A_{\chi,r}^{(p),C}(\theta, \varphi)$, several different and available state-of-the-art techniques could be employed, but since the excitations $\mathbf{w}_{\chi,r}^{(p)}$ must be computed in real time for each (χ, r) -beam ($\chi \in \{V, H\}$; $r = 1, \dots, R$) and for every Green’s function variation [i.e., p -th ($p = 1, \dots, P$) propagation scenario], the *ZF* scheme is adopted [6][11][12]. As a matter of fact, although sub-optimal, it guarantees a computationally-inexpensive maximization of $\mathcal{C}_{\chi,r}^{(p)}$ ($\chi \in \{V, H\}$, $r = 1, \dots, R$) by enforcing $\mu_{\chi,r}^{(p)} = 0$ in (3) (i.e., no *intra-cell multi-user interference*) [11][12]. More in detail, the overall excitation set $\mathcal{W}^{(p),C} \triangleq \{\mathbf{w}_{\chi,r}^{(p),C}; \chi \in \{V, H\}, r = 1, \dots, R\}$ is defined as follows

$$\mathcal{W}^{(p),C} = [\mathcal{G}^{(p)}]^\dagger \quad (8)$$

where $\mathcal{G}^{(p)} \triangleq \{\mathbf{g}_{\chi,r}^{(p)}; r = 1, \dots, R; \chi \in \{V, H\}\}$ is the Green’s frequency-domain complex matrix, and the apex \cdot^\dagger stands for the Moore-Penrose pseudo-inverse operator (i.e., $\mathcal{G}^\dagger \triangleq \mathcal{G}^* [\mathcal{G}\mathcal{G}^*]^{-1}$, \cdot^* being the conjugate transpose operator). Successively, the patterns set $\{A_{\chi,r}^{(p),C}(\theta, \varphi); \chi \in \{V, H\}; r = 1, \dots, R; p = 1, \dots, P\}$ is derived by applying the pattern/excitation transformation operator to the *ZF*-based excitations $A_{\chi,r}^{(p),C}(\theta, \varphi) = \mathcal{F} \left[\mathbf{w}_{\chi,r}^{(p),C} \right]$.

The setting of $A_{\chi,r}^{(p),\mathcal{I}}(\theta, \varphi)$ to mitigate the out-of-sector total interference can be also yielded with different standard methods [7]. To keep low the computational complexity, while maximizing the radiation efficiency and decreasing the sidelobe envelope to indirectly mitigate \mathcal{I}_{ave} [7], an isophoric (*ISO*) excitation synthesis scheme [6] is adopted. Accordingly, the auxiliary pattern $A_{\chi,r}^{(p),\mathcal{I}}(\theta, \varphi)$ ($\chi \in \{V, H\}; r = 1, \dots, R; p = 1, \dots, P$) is set to that radiated by the excitation vector $\mathbf{w}_{\chi,r}^{(p),\mathcal{I}}$ (i.e., $A_{\chi,r}^{(p),\mathcal{I}}(\theta, \varphi) = \mathcal{F}[\mathbf{w}_{\chi,r}^{(p),\mathcal{I}}]$) whose (t, ψ) -th ($t = 1, \dots, T; \psi \in \{V, H\}$) entry is equal to

$$w_{\chi,\psi,r,t}^{(p),\mathcal{I}} = \exp[\Phi_{tr}] \quad (9)$$

Φ_{tr} being the phase term that enables the χ -polarized ($\chi \in \{V, H\}$) beam to be steered towards the r -th ($r = 1, \dots, R$) receiver location $\underline{\rho}_r$ [6] (i.e., $\Phi_{tr} \triangleq \frac{2\pi f}{c_0} \left(\frac{\underline{\rho}_t \cdot (\underline{\rho}_r - \underline{\rho}_t)}{|\underline{\rho}_r - \underline{\rho}_t|} \right)$).

It is worth pointing out that, since the *HCS* approach does not depend on the methodologies to compute $A_{\chi,r}^{(p),\mathcal{C}}(\theta, \varphi)$ and $A_{\chi,r}^{(p),\mathcal{I}}(\theta, \varphi)$, but rather on these latter as reference for the next steps, more computationally-intensive strategies can be seamlessly adopted instead of (8) and (9) according to the available computational resources and desired performance.

Analogously, the process (Step 2) to define the hybrid pattern $\tilde{A}_{\chi,r}^{(p)}(\theta, \varphi)$ ($\chi \in \{V, H\}, r = 1, \dots, R, p = 1, \dots, P$), starting from the references $A_{\chi,r}^{(p),\mathcal{C}}(\theta, \varphi)$ and $A_{\chi,r}^{(p),\mathcal{I}}(\theta, \varphi)$ of Step 1, can be implemented in different ways. Owing to the guidelines discussed above, a very simple solution would be preferred, thus a straightforward piecewise approximation is chosen

$$\tilde{A}_{\chi,r}^{(p)}(\theta, \varphi) \triangleq \begin{cases} A_{\chi,r}^{(p),\mathcal{C}}(\theta, \varphi) & \{\theta, \varphi\} \in \Xi \\ A_{\chi,r}^{(p),\mathcal{I}}(\theta, \varphi) & \{\theta, \varphi\} \notin \Xi \end{cases}. \quad (10)$$

Since (10) may generate a non-continuous target pattern, the exact matching between $A_{\chi,r}^{(p)}(\theta, \varphi)$ and $\tilde{A}_{\chi,r}^{(p)}(\theta, \varphi)$ is inherently prevented because of the finite number of the *BS* array elements. Therefore, the excitations synthesis in the Step 3 is then aimed at finding $\mathbf{w}_{\chi,r}^{(p)}$ so that the afforded pattern $A_{\chi,r}^{(p)}(\theta, \varphi)$ is an approximation of the hybrid and ideal one, $A_{\chi,r}^{(p)}(\theta, \varphi) \approx \tilde{A}_{\chi,r}^{(p)}(\theta, \varphi)$, for each (χ, r) -beam ($\chi \in \{V, H\}; r = 1, \dots, R$) and p -th ($p = 1, \dots, P$) scenario. Following this guideline, a simple, elegant, and insightful approach based on the Woodward-Lawson (*WL*) beam shaping technique [8] is exploited since (i) it only needs the samples of the

desired pattern at various discrete locations, (ii) it is simple to implement, (iii) it is extremely computationally-efficient, and (iv) it does not imply any iterative processing unlike most alternative techniques [8][15] including deterministic [20] or stochastic [19] strategies.

Under the assumption of regularly-spaced antennas [e.g., $\rho_t \triangleq (0, (t - \frac{T-1}{2}) \times d, 0)$ ($t = 1, \dots, T$), d being inter-element spacing - Fig. 1] and negligible edge effects (i.e., $E_{\psi,t}(\theta, \varphi) \approx E_{\psi}(\theta, \varphi)$, $\psi \in \{V, H\}$), the final array excitations are obtained as follows [8]

$$w_{\chi,\psi,r,t}^{(p)} = \sum_{q=1}^T \left\{ \frac{\tilde{A}_{\chi,r}^{(p)}(\theta_q, \varphi_q)}{E_{\psi}(\theta_q, \varphi_q)} \exp \left[-j \frac{2\pi f}{c_0} (y_t \sin \theta_q \sin \varphi_q) \right] \right\} \quad (11)$$

($\chi, \psi \in \{V, H\}$; $r = 1, \dots, R$; $t = 1, \dots, T$) where (θ_q, φ_q) are the q -th ($q = 1, \dots, Q$) angular coordinates of azimuth pattern samples. Thanks to (11), while generally $A_{\chi,r}^{(p)}(\theta, \varphi) \approx \tilde{A}_{\chi,r}^{(p)}(\theta, \varphi)$, the matching is ideal at the Q sampling angles [8], $A_{\chi,r}^{(p)}(\theta_q, \varphi_q) = \tilde{A}_{\chi,r}^{(p)}(\theta_q, \varphi_q)$ ($q = 1, \dots, Q$). In summary, the proposed beamforming scheme solves the *COIM* problem by combining (8), (9), (10), and (11). Consequently, the computational complexity of the *HCS* method only slightly increases that of the popular and efficient *ZF* scheme [11][12] since the additional computations are concerned with a closed-form isophoric weighting (9), a piecewise pattern combination (10), and a closed-form *WL* synthesis (11). Moreover, it is worth pointing out that the *HCS* method does not feature any configuration parameter, thus potential calibration and robustness issues are avoided by definition.

4 Numerical Assessment

This section is aimed at illustrating the application of the *HCS* array synthesis method, at providing suitable guidelines for an effective use in practical scenarios, and at assessing the achievable performance in terms of capacity maximization and inter-cell interference mitigation also in comparison with state-of-the-art beamforming techniques for massive *MIMO* processing and canonical array synthesis approaches [6][8]. Towards this end, different propagation scenarios (Fig. 2), number of transmitting/receiving antennas, and signal-to-noise ratio (*SNR*) conditions have been considered, while the Green's function for each scenario has been computed with a geometry-based stochastic method that exploits an approximated ray-tracing approach [12]

implemented in the *QuaDRiGa* physical-channel simulator [1][21]-[23].

The first numerical experiment deals with a urban micro-cellular scenario (*UMi*) where $R = 16$ terminals, equipped with dual-polarization patch antennas, are served by a *BS MIMO* array, consisting of $T = 16$ $d = \frac{\lambda}{2}$ -spaced patches featuring ± 45 [deg] polarization, located 10 [m] above the ground. Moreover, the coverage cell extends from $\varphi_{\min} = -60$ [deg] up to $\varphi_{\max} = +60$ [deg]. As in [12][6], the propagation environment has been modeled according to the so-called *Madrid grid* [“Scenario 1” - Fig. 2(a)] and a generalized International Mobile Telecommunications-Advanced (*IMT-A*) setup (*NLOS IMT-A UMi*) has been simulated at $f = 2.0$ GHz with *QuaDRiGa* [21]-[23], by setting $P = 100$ and $SNR = 20$ [dB] ($SNR \triangleq \frac{\sigma}{\sigma^2}$). In Fig. 3(a), the plots of the average capacity across P random scenarios, $\mathcal{C}_{\chi,r}$ ($\mathcal{C}_{\chi,r} \triangleq \frac{1}{P} \sum_{p=1}^P \mathcal{C}_{\chi,r}^{(p)}$) of the (χ, r) -beam ($\chi \in \{V, H\}$; $r = 1, \dots, R$) yielded with the *HCS* (11), the *ZF* (8), and the *ISO* (9) methods are reported. As theoretically expected [6], the *ZF* approach guarantees the maximum communication performance regardless of the beam index and the polarization state ($\Delta \mathcal{C}_{\chi,r}^{ZF-ISO} \in [3.2 \times 10^1, 1.3 \times 10^5]$ being $\Delta \mathcal{C}_{\chi,r}^{ZF-ISO} \triangleq \frac{\mathcal{C}_{\chi,r}^{ZF}}{\mathcal{C}_{\chi,r}^{ISO}}$) thanks to a constructive exploitation of the propagation scenario to increase the end-to-end information transfer. On the other hand, while the *ZF* significantly outperforms the *ISO* method in terms of average capacity ($\mathcal{C}_{ave}^{ZF} \approx 187.75$ [bps/Hz] vs. $\mathcal{C}_{ave}^{ISO} \approx 1.55$ [bps/Hz] - Tab. I), the performance of the *HCS* turns out are very close to the *ZF* one ($\Delta \mathcal{C}_{\chi,r}^{HCS-ZF} \in [0.57, 0.86]$) and better than that from the *ISO* approach ($\Delta \mathcal{C}_{\chi,r}^{HCS-ISO} \in [2.2 \times 10^1, 1.0 \times 10^5]$). This trend is also confirmed by the corresponding overall average capacity indexes ($\Delta \mathcal{C}_{ave}^{ZF-HCS} \approx 1.44$ vs. $\Delta \mathcal{C}_{ave}^{ISO-HCS} \approx 1.19 \times 10^{-2}$ - Tab. I). But what about the inter-cell interference of the radiated pattern? The results in Fig. 3(b) indicate that the *HCS* technique improves the average out-of-sector interference $\mathcal{I}_{\chi,r}$ ($\mathcal{I}_{\chi,r} \triangleq \frac{1}{P} \sum_{p=1}^P \mathcal{I}_{\chi,r}^{(p)}$) of the *ZF* approach (i.e., $\mathcal{I}_{\chi,r}^{ZF} \in [-16.3, -8.1]$ [dB] vs. $\mathcal{I}_{\chi,r}^{HCS} \in [-28.0, -15.9]$ [dB]) with values not far from those of the *ISO* method being $\mathcal{I}_{\chi,r}^{ISO} \in [-27.6, -25.4]$ [dB]. Such an outcome is further pointed out by the per-beam interference mitigation difference, $\Delta \mathcal{I}_{\chi,r}^{ZF-HCS}$ ($\Delta \mathcal{I}_{\chi,r}^{ZF-HCS} \triangleq \mathcal{I}_{\chi,r}^{ZF} - \mathcal{I}_{\chi,r}^{HCS}$), since $\Delta \mathcal{I}_{\chi,r}^{ZF-HCS} \in [6.2, 16.4]$ [dB], and from the corresponding average interference indexes in Tab. I. Vice-versa, the average per-beam directivity $\mathcal{D}_{\chi,r}$ ($\mathcal{D}_{\chi,r} \triangleq \frac{1}{P} \sum_{p=1}^P \mathcal{D}_{\chi,r}^{(p)}$, $\mathcal{D}_{\chi,r}^{(p)}$ being the directivity of the (χ, r) -beam ($\chi \in \{V, H\}$, $r = 1, \dots, R$) at frequency f in the p -th ($p = 1, \dots, P$) scenario) as

well as the overall directivity ($\Delta\mathcal{D}_{\chi,r}^{ISO-HCS} \approx 8.2$ [dB], being $\Delta\mathcal{D}_{\chi,r}^{ISO-HCS} \triangleq \mathcal{D}_{ave}^{ISO} - \mathcal{D}_{ave}^{HCS}$ - Tab. I) of both the *HCS* and the *ZF* approaches is considerably lower than that of the *ISO* method [Fig. 3(c)] as theoretically known [6]. As a matter of fact, the *HCS* beams exhibit distorted shapes with multi-lobes within the *BS* angular sector, while the sidelobes are well-controlled in the out-of-sector angular directions as pictorially shown in Fig. 6(c) for a representative case ($r = 19$). For completeness and illustrative purposes, let us analyze the behaviour of the patterns $A_{\chi,r}^{(p),C}(\theta, \varphi)$, $A_{\chi,r}^{(p),I}(\theta, \varphi)$, and $A_{\chi,r}^{(p)}(\theta, \varphi)$ along the $\theta = 90$ [deg]-cut (Fig. 5) radiated by the transmitting *BS* when serving the ($r = 19$)-th receiver using the excitations in Fig. 4. One can notice that the *HCS* technique carefully approximates the *ZF* beam within the in-sector angular region, while it matches the *ISO* pattern outside to reduce the sidelobes when $\varphi \leq \varphi_{\min}$ or $\varphi \geq \varphi_{\max}$ [Figs. 5(a)-5(b)]. Moreover, the $A_{\chi,r}^{(p)}(\theta_q, \varphi_q)$ exactly passes through the matching samples $\tilde{A}_{\chi,r}^{(p)}(\theta_q, \varphi_q)$ [i.e., blue line vs. black dots in Figs. 5(a)-5(b)] as required by the *WL* formulation.

The same conclusions are expected regardless of the users location and their distributions. For a check, the second experiment is concerned with the same *BS* arrangement of the first example, but assuming the propagation setup shown in Fig. 2(b) (“*Scenario 2*”) instead of that modeled by the “*Scenario 1*” [Fig. 2(a)]. The plots of the average capacity $\mathcal{C}_{\chi,r}$ [Fig. 7(a)] and of the average out-of-sector interference $\mathcal{I}_{\chi,r}$ [Fig. 7(b)] confirm that the *HCS* method synthesizes radiation patterns featuring an almost optimal information transfer [i.e., $\mathcal{C}_{\chi,r}^{ZF} \approx \mathcal{C}_{\chi,r}^{HCS}$ - Fig. 7(a)] and reduced inter-sector interferences [i.e., $\mathcal{I}_{\chi,r}^{ZF} \approx \mathcal{I}_{\chi,r}^{HCS}$ - Fig. 7(a)] with respect to the *ZF* approach, while it outperforms the *ISO* scheme in terms of per-beam and average capacity [i.e., $\mathcal{C}_{\chi,r}^{ISO} < \mathcal{C}_{\chi,r}^{HCS}$ - Fig. 7(a)], as confirmed by the values of the overall performance indexes ($\Delta\mathcal{C}_{ave}^{ZF-HCS} \approx 2.2$ vs. $\Delta\mathcal{C}_{ave}^{ISO-HCS} \approx 1.8 \times 10^{-2}$; $\Delta\mathcal{I}_{ave}^{ZF-HCS} \approx 10$ [dB] - Tab. II), as well. On the other hand and once again, the *HCS* array yields values of $\mathcal{D}_{\chi,r}$ smaller than those from the *ISO* one [Fig. 7(c)] because of multi-lobes pattern within the in-sector region ($\varphi_{\min} \leq \varphi \leq \varphi_{\max}$) as visualized by the plots of both the 2D-cuts [Figs. 8(e)-Fig. 8(f)] and the 3D distributions [Fig. 9(c) vs. Figs. 9(a)-9(b)] of the normalized power patterns $A_{\chi,r}^{(p),C}(\theta, \varphi)$, $A_{\chi,r}^{(p),I}(\theta, \varphi)$, and $A_{\chi,r}^{(p)}(\theta, \varphi)$ afforded by the excitations reported in Figs. 8(a)-8(d) and related to the $r = 1$ beam.

The next numerical experiment is aimed at assessing the effectiveness of the *HCS* paradigm as well as the dependence of its performance on the number of transmitters, T , in the *BS*. With reference to the “*Scenario I*” [Fig. 2(a)], Figure 10 shows the behavior of \mathcal{C}_{ave} [Fig. 10(a)], \mathcal{I}_{ave} [Fig. 10(b)], and \mathcal{D}_{ave} versus T . As it can be inferred from the plots, it turns out that (i) the interference mitigation capabilities of all techniques increase when the array enlarges [Fig. 10(b)]; (ii) the *HCS* technique achieves capacity values very close to those with the *ZF* scheme regardless of the *BS* size [i.e., $\Delta\mathcal{C}_{ave}^{ZF-HCS} \approx 1.3$ - Fig. 10(a)], but it improves the *ZF* interference-mitigation features of about 10 [dB] [Fig. 10(b)]; (iii) the *HCS* synthesis effectively and profitably exploits the additional degrees-of-freedom of wider apertures by improving both the downlink capacity and the interference suppression [Fig. 10(a) and Fig. 10(b)]; (iv) the free-space directivity of capacity-oriented strategies [Fig. 10(c)] does not significantly improve when using larger apertures since focusing the beam towards the receiver is known to be a strongly sub-optimal capacity-maximization strategy when realistic/multi-path propagation scenarios are at hand [6].

The dependence of the performance indexes on the number of receiving terminals R has been analyzed next by keeping the scenario in Fig. 2(a) and setting $T = 72$. In Fig. 11, the plots of \mathcal{C}_{ave} , \mathcal{I}_{ave} , and \mathcal{D}_{ave} as a function of R are reported. As already proven in [6], the *ZF* sum-rate capacity does not monotonically enhance with R because of the unavoidable growth of the intra-cell multi-user interference $\mu_{\chi,r}^{(p)}$ when the user density increases, which causes a reduction of the propagation diversity of the associated Green’s functions [Fig. 11(a)]. As expected, a similar trend arises when applying the *HCS* [i.e., $\Delta\mathcal{C}_{ave}^{ZF-HCS} \in [1.25, 4.5]$ - Fig. 11(a)]. The dependence of \mathcal{I}_{ave} on the number of receivers is also similar between *HCS* and *ZF* methods, even though the former/hybrid one still strongly outperforms the other [$\Delta\mathcal{I}_{ave}^{ZF-HCS} \in [8, 10]$ [dB] - Fig. 11(b)]. As for the comparison between the *HCS* and the *ISO* performance, the same outcomes from the analysis versus T can be drawn [Fig. 11(c)].

The final numerical test is aimed at evaluating the proposed synthesis scheme when dealing with different propagation models and *SNR* values. More specifically, the *QuaDRiGa* SW tool [21][22][23] has been configured to numerically compute the Green’s functions of a rural scenario with/without line-of-sight propagation conditions according to the *LOS 3GPP RMa*

and the *NLOS 3GPP RMa* models [24], respectively. Accordingly, \mathcal{C}_{ave} and \mathcal{I}_{ave} have been computed in the benchmark $T = 32$, $R = 16$ setup by varying the *SNR* within the range $SNR \in [10, 40]$ [dB] (Fig. 12). For comparison purposes, the values for the *NLOS IMT-A UMi* scenario are reported, as well. Notwithstanding the propagation scenario and the noisy conditions, the *HCS* further confirms its effectiveness as optimal trade-off in terms of average downlink capacity [\mathcal{C}_{ave} - Fig. 12(a)] and out-of-sector interference ratio [\mathcal{I}_{ave} - Fig. 12(b)] with respect to the other approaches. Moreover, it is worth noticing that, even in rural scenarios and partially line-of-sight propagation (i.e., *LOS 3GPP RMa*), the capacity values yielded by the *ISO* technique are considerably smaller than those of the *HCS* method [Fig. 12(a)]. Such a result remarks that, as expected [6], purely free-space oriented beamforming techniques such as (9) does not optimally transfer information also when low-scattering environments with line-of-sight conditions are at hand [Fig. 12(a)].

Of course, besides the trade-off optimality, the simplicity and the computational efficiency are expected to be the other key features of the proposed synthesis scheme. For assessment purposes, the average overall synthesis time τ [$\tau \triangleq \frac{1}{P} \sum_{p=1}^P \tau^{(p)}$, $\tau^{(p)}$ being the time spent for synthesizing the (χ, r) -beam ($\chi \in \{V, H\}$; $r = 1, \dots, R$) excitations in the p -th ($p = 1, \dots, P$) scenario: $\tau^{(p)} = \sum_{\chi=V,H} \sum_{r=1}^R \tau_{\chi,r}^{(p)}$] required by the *ZF*, the *ISO*, and the *HCS* methods when dealing with different setups of transmitters, T , and receivers, R , has been reported in Fig. 13. For the sake of fairness, all the *CPU*-times refer to non-optimized Matlab implementations executed on a single-core laptop PC with 1.60 GHz-running *CPU*.

As a representative test case, first the case of $R = 16$ receivers located as in Fig. 2(a) has been analyzed. Figure 13(a) shows that, whatever the synthesis method, the synthesis time τ slightly increases as the size of the transmitting antenna widens (e.g., $\delta\tau^{ISO} \approx 1.02$, $\delta\tau^{ZF} \approx 1.05$, and $\delta\tau^{HCS} \approx 1.04$ being $\delta\tau \triangleq \frac{\tau|_{T=104}}{\tau|_{T=32}}$). More important, the synthesis time for the *HCS* is close to that of the *ZF* scheme (e.g., $\Delta\tau^{HCS-ZF} \approx 1.19$ being $\Delta\tau^{HCS-ZF} \triangleq \frac{\tau^{HCS}|_{T=104}}{\tau^{ZF}|_{T=104}}$), which is widely recognized as the most numerically efficient and easy to implement approach [6][11][12]. Such a result is not surprising since it has been actually anticipated in Sect. 3 from the theoretical perspective. Indeed, the *HCS* implementation needs only closed-form steps (i.e., an isophoric weighting, a pattern combination, and a *WL* synthesis) besides *ZF* one. For

completeness, the results from the numerical test with $T = 72$ transmitters and varying the number of receivers, R , are given in Fig. 13(b). Despite a different dependence of the *CPU*-time on the number of terminals R with respect to the number of transmitting elements T , it is confirmed that the *HCS* implementation is simple and scalable with a computational cost comparable to that of the popular *ZF* paradigm, therefore a suitable solution when real-time processing is required.

5 Conclusions

An innovative pattern synthesis technique has been proposed for the real-time *MIMO* array control when capacity-oriented radiation performance, out-of-cell sidelobe reduction, and low-complexity processing are simultaneously required. Such an approach is based on a non-iterative hybrid scheme where, for each beam, two auxiliary sets of excitations and the associated patterns are firstly synthesized, then an ideal hybrid pattern is derived from their angular combination so that the final array excitations are determined to radiate the best angular approximation of this latter one. A set of representative results, from a wide numerical analysis, has been presented to discuss on the features and the potentialities of the proposed *HCS* synthesis as well as to assess its performance in terms of downlink capacity, interference control, and computational efficiency in comparison with other state-of-the-art popular beamforming methods, as well.

To the best of the authors' knowledge, the main methodological advancements of the paper with respect to the reference literature on the topic include (i) the introduction of a computationally-efficient excitation synthesis method suitable for jointly handling the capacity-maximization and the out-of-sector interference mitigation; (ii) the derivation of a real-time beamforming procedure that, thanks to its modularity, can be easily extended to exploit additional computational resources and/or more advanced/expensive single-step methods as well as to account for additional requirements arising in next-generation massive *MIMO* scenarios (e.g., static/dynamic jamming rejection, null positioning); (iii) the numerical assessment of the proposed approach in comparison with widely-adopted capacity-driven and sidelobe-minimizing methods, as well, as a mandatory step for deriving suitable guidelines towards a practical implementation of the

HCS strategy.

The numerical validation has shown that

- the use of the *HCS* method implies a negligible capacity reduction with respect to the popular *ZF* algorithm regardless of the propagation scenario, number of transmitters and receivers, and noise level, while always outperforming the *ISO* performance;
- the *HCS* considerably reduces the out-of-sector interferences occurring when adopting the *ZF* approach [Fig. 2(b)] thanks to an effective shaping/control of the out-of-sector secondary lobes;
- the *HCS* does not need calibration, notwithstanding the change of the propagation scenario or noisy conditions, owing to the absence of control parameters;
- the computational complexity of the *HCS* is similar to that of the *ZF* scheme, thus suitable for real-time operative conditions.

Future works, beyond the scope of the present paper, will be aimed at generalizing the *HCS* scheme to different array architectures (e.g., sparse, thinned, clustered, overlapped, etc.) and geometries (e.g., planar, conformal). Customizations to deal with additional requirements and applicative guidelines in terms of both intra- and inter-cell performance are also envisaged.

Acknowledgements

This work benefited from the networking activities carried out within the Project “Cloaking Metasurfaces for a New Generation of Intelligent Antenna Systems (MANTLES)” (Grant No. 2017BHFZKH) funded by the Italian Ministry of Education, University, and Research under the PRIN2017 Program (CUP: E64I19000560001), and within the Project “SPEED” (Grant No. 61721001) funded by the National Science Foundation of China under the ChangJiang Visiting Professorship Program. A. Massa wishes to thank E. Vico for her never-ending inspiration, support, guidance, and help.

References

- [1] T. S. Rappaport, Y. Xing, G. R. MacCartney, A. F. Molisch, E. Mellios, and J. Zhang, "Overview of millimeter wave communications for fifth-generation (5G) wireless networks with a focus on propagation models," *IEEE Trans. Antennas Propag.*, vol. 65, no. 12, pp. 6213-6230, Dec. 2017.
- [2] W. Hong, Z. H. Jiang, C. Yu, J. Zhou, P. Chen, Z. Yu, H. Zhang, B. Yang, X. Pang, M. Jiang, Y. Cheng, M. K. T. Al-Nuaimi, Y. Zhang, J. Chen, and S. He, "Multibeam Antenna Technologies for 5G Wireless Communications," *IEEE Trans. Antennas Propag.*, vol. 65, no. 12, pp. 6231-6249, Dec. 2017.
- [3] D. Liu, W. Hong, T. S. Rappaport, C. Luxey, and W. Hong, "What will 5G antennas and propagation be?," *IEEE Trans. Antennas Propag.*, vol. 65, no. 12, pp. 6205-6212, Dec. 2017.
- [4] G. Oliveri, G. Gottardi, F. Robol, A. Polo, L. Poli, M. Salucci, M. Chuan, C. Massagrande, P. Vinetti, M. Mattivi, R. Lombardi, and A. Massa, "Co-design of unconventional array architectures and antenna elements for 5G base stations," *IEEE Trans. Antennas Propag.*, vol. 65, no. 12, pp. 6752- 6766, Dec. 2017.
- [5] C. Mao, S. Gao, and Y. Wang, "Broadband high-gain beam-scanning antenna array for millimeter-wave applications," *IEEE Trans. Antennas Propag.*, vol. 65, no. 9, pp. 4864-4868, Sept. 2017.
- [6] G. Oliveri, G. Gottardi, and A. Massa, "A new meta-paradigm for the synthesis of antenna arrays for future wireless communications," *IEEE Trans. Antennas Propag.*, vol. 67, no. 6, pp. 3774-3788, Jun. 2019.
- [7] R. J. Mailloux, *Phased Array Antenna Handbook*. Boston, MA: Artech House, 2005.
- [8] C. A. Balanis, *Antenna Theory, Analysis and Design*, 2nd ed., New York: Wiley, 1997.

- [9] N. Shinohara, "Beam control technologies with a high-efficiency phased array for microwave power transmission in Japan," *Proc. IEEE*, vol. 101, no. 6, pp. 1448-1463, Jun. 2013.
- [10] G. Oliveri, L. Poli, and A. Massa, "Maximum efficiency beam synthesis of radiating planar arrays for wireless power transmission," *IEEE Trans. Antennas Propag.*, vol. 61, no. 5, pp. 2490-2499, May 2013.
- [11] F. Kaltenberger, D. Gesbert, R. Knopp, and M. Kountouris, "Correlation and capacity of measured multi-user MIMO channels," in *2008 IEEE 19th Int. Symp. Personal, Indoor and Mobile Radio Comm.*, Cannes, France, 2008, pp. 1-5.
- [12] P. Kyosti, J. Lehtomaki, J. Medbo, and M. Latva-aho, "Map-based channel model for evaluation of 5G wireless communication systems," *IEEE Trans. Antennas Propag.*, vol. 65, no. 12, pp. 6491-6504, Dec. 2017.
- [13] P. Rocca, G. Oliveri, R. J. Mailloux, and A. Massa, "Unconventional phased array architectures and design methodologies - A review," *Proc. IEEE*, vol. 104, no. 3, pp. 544-560, Mar. 2016.
- [14] J. Robinson and Y. Rahmat-Samii, "Particle swarm optimization in electromagnetics," *IEEE Trans. Antennas Propag.*, vol. 52, no. 2, pp. 397-407, Feb. 2004.
- [15] P. Rocca, M. Benedetti, M. Donelli, D. Franceschini, and A. Massa, "Evolutionary optimization as applied to inverse scattering problems," *Inverse Probl.*, vol. 25, no. 12, pp. 1-41, Dec. 2009.
- [16] P. Rocca, G. Oliveri, and A. Massa, "Differential evolution as applied to electromagnetics," *IEEE Antennas Propag. Mag.*, vol. 53, no. 1, pp. 38-49, Feb. 2011.
- [17] N. Jin and Y. Rahmat-Samii, "Advances in particle swarm optimization for antenna designs: real-number, binary, single-objective and multiobjective implementations," *IEEE Trans. Antennas Propag.*, vol. 55, no. 3, pp. 556-567, Mar. 2007.

- [18] D. H. Wolpert and W. G. J. Macready, "No free lunch theorems for optimization," *IEEE Trans. Evol. Comput.*, vol. 1, no. 1, pp. 67-82, Apr. 1997.
- [19] R. L. Haupt, "Optimized weighting of uniform subarrays of unequal size," *IEEE Trans. Antennas Propag.*, vol. 55, no. 4, pp. 1207-1210, Apr. 2007.
- [20] H. J. Orchard, R. S. Elliott, and G. J. Stern, "Optimising the synthesis of shaped beam antenna patterns," *IEE Proc. H*, vol. 132, no. 1, pp. 63-68, Feb. 1985.
- [21] S. Jaeckel, K. Borner, L. Thiele, and V. Jungnickel, "A geometric polarization rotation model for the 3-D spatial channel model," *IEEE Trans. Antennas Propag.*, vol. 60, no. 12, pp. 5966-5977, Dec. 2012.
- [22] S. Jaeckel, L. Raschkowski, K. Borner, and L. Thiele, "QuaDRiGa: a 3-D multi-cell channel model with time evolution for enabling virtual field trials," *IEEE Trans. Antennas Propag.*, vol. 62, no. 6, pp. 3242-3256, Jun. 2014.
- [23] S. Jaeckel, *Quasi-deterministic channel modeling and experimental validation in cooperative and massive MIMO deployment topologies*, Ph.D. Dissertation, TU Ilmenau, Ilmenau, 2017.
- [24] 3GPP RAN 1 Working Group, "Study on channel model for frequencies from 0.5 to 100 GHz," Tech Rep. TR 38.901, Jun. 2017.

FIGURE CAPTIONS

- **Figure 1.** *Problem Geometry.* Multi-user multi-antenna downlink communication.
- **Figure 2.** *Benchmark Environments* (“Madrid Grid” urban environment, *NLOS IMT-A UMi* model). Location of the *BS* antenna (i.e., a transmitting array of S radiating elements) and of the L terminals in (a) the “*Scenario 1*” and (b) the “*Scenario 2*”.
- **Figure 3.** *Numerical Assessment (NLOS IMT-A UMi model - Scenario 1, $T = 32, R = 16, SNR = 20$ [dB], $P = 100$).* Behaviour of (a) $\mathcal{C}_{\chi,r}$, (b) $\mathcal{I}_{\chi,r}$, and (c) $\mathcal{D}_{\chi,r}$ versus the r -th ($r = 1, \dots, R$) receiver index ($\chi \in \{V, H\}$).
- **Figure 4.** *Numerical Assessment (NLOS IMT-A UMi model - Scenario 1, $T = 32, R = 16, SNR = 20$ [dB], $r = 19, p = 1$).* Plots of (a)(b) the magnitude and (c)(d) the phase of $w_{\chi,\psi,r,t}^{(p)}$ versus the t -th ($t = 1, \dots, T$) array element index when (a)(c) $\chi = \psi = V$ and (b)(d) $\chi = \psi = H$.
- **Figure 5.** *Numerical Assessment (NLOS IMT-A UMi model - Scenario 1, $T = 32, R = 16, SNR = 20$ [dB], $r = 19, p = 1$).* Normalized magnitude of $A_{\chi,r}^{(p),C}(\theta, \varphi)$, $A_{\chi,r}^{(p),\mathcal{I}}(\theta, \varphi)$, and $A_{\chi,r}^{(p)}(\theta, \varphi)$ along the $\theta = 90$ [deg]-cut when (a) $\chi = \psi = V$ and (b) $\chi = \psi = H$.
- **Figure 6.** *Numerical Assessment (NLOS IMT-A UMi model - Scenario 1, $T = 32, R = 16, SNR = 20$ [dB], $r = 19, p = 1, \chi = \psi = V$).* Normalized 3D magnitude of (a) $A_{\chi,r}^{(p),C}(\theta, \varphi)$, (b) $A_{\chi,r}^{(p),\mathcal{I}}(\theta, \varphi)$, and (c) $A_{\chi,r}^{(p)}(\theta, \varphi)$.
- **Figure 7.** *Numerical Assessment (NLOS IMT-A UMi model - Scenario 2, $T = 32, R = 16, SNR = 20$ [dB], $P = 100$).* Behaviour of (a) $\mathcal{C}_{\chi,r}$, (b) $\mathcal{I}_{\chi,r}$, and (c) $\mathcal{D}_{\chi,r}$ versus the r -th ($r = 1, \dots, R$) receiver index ($\chi \in \{V, H\}$).
- **Figure 8.** *Numerical Assessment (NLOS IMT-A UMi model - Scenario 2, $T = 32, R = 16, SNR = 20$ [dB], $r = 19, p = 1$).* Plots of (a)(b) the magnitude and (c)(d) the phase of $w_{\chi,\psi,r,t}^{(p)}$ versus the t -th ($t = 1, \dots, T$) element index, and of (e)(f) the normalized

magnitude of $A_{\chi,r}^{(p),\mathcal{C}}(\theta, \varphi)$, $A_{\chi,r}^{(p),\mathcal{I}}(\theta, \varphi)$, and $A_{\chi,r}^{(p)}(\theta, \varphi)$ along the $\theta = 90$ [deg]-cut when (a)(c)(e) $\chi = \psi = V$ or (b)(d)(f) $\chi = \psi = H$.

- **Figure 9.** Numerical Assessment (NLOS IMT-A UMi model - Scenario 2, $T = 32$, $R = 16$, $SNR = 20$ [dB], $r = 19$, $p = 1$, $\chi = \psi = V$). Normalized 3D magnitude of (a) $A_{\chi,r}^{(p),\mathcal{C}}(\theta, \varphi)$, (b) $A_{\chi,r}^{(p),\mathcal{I}}(\theta, \varphi)$, and (c) $A_{\chi,r}^{(p)}(\theta, \varphi)$.
- **Figure 10.** Numerical Assessment (NLOS IMT-A UMi model - Scenario 1, $R = 16$, $SNR = 20$ [dB]). Behaviour of (a) \mathcal{C}_{ave} , (b) \mathcal{I}_{ave} , and (c) \mathcal{D}_{ave} versus T .
- **Figure 11.** Numerical Assessment (NLOS IMT-A UMi model - Scenario 1, $T = 72$, $SNR = 20$ [dB]). Behaviour of (a) \mathcal{C}_{ave} , (b) \mathcal{I}_{ave} , and (c) \mathcal{D}_{ave} versus R .
- **Figure 12.** Numerical Assessment ($S = 32$, $L = 16$). Behaviour of (a) \mathcal{C}_{ave} and (b) \mathcal{I}_{ave} versus SNR .
- **Figure 13.** Numerical Assessment (NLOS IMT-A UMi model - Scenario 1, $SNR = 20$ [dB]). Behaviour of τ^{ZF} , τ^{ISO} , and τ^{HCS} (a) versus T ($R = 16$) and (b) versus R ($T = 72$).

TABLE CAPTIONS

- **Table I.** Numerical Assessment (NLOS IMT-A UMi model - Scenario 1, $T = 32$, $R = 16$, $SNR = 20$ [dB], $P = 100$). Average performance indexes.
- **Table II.** Numerical Assessment (NLOS IMT-A UMi model - Scenario 2, $T = 32$, $R = 16$, $SNR = 20$ [dB], $P = 100$). Average performance indexes.

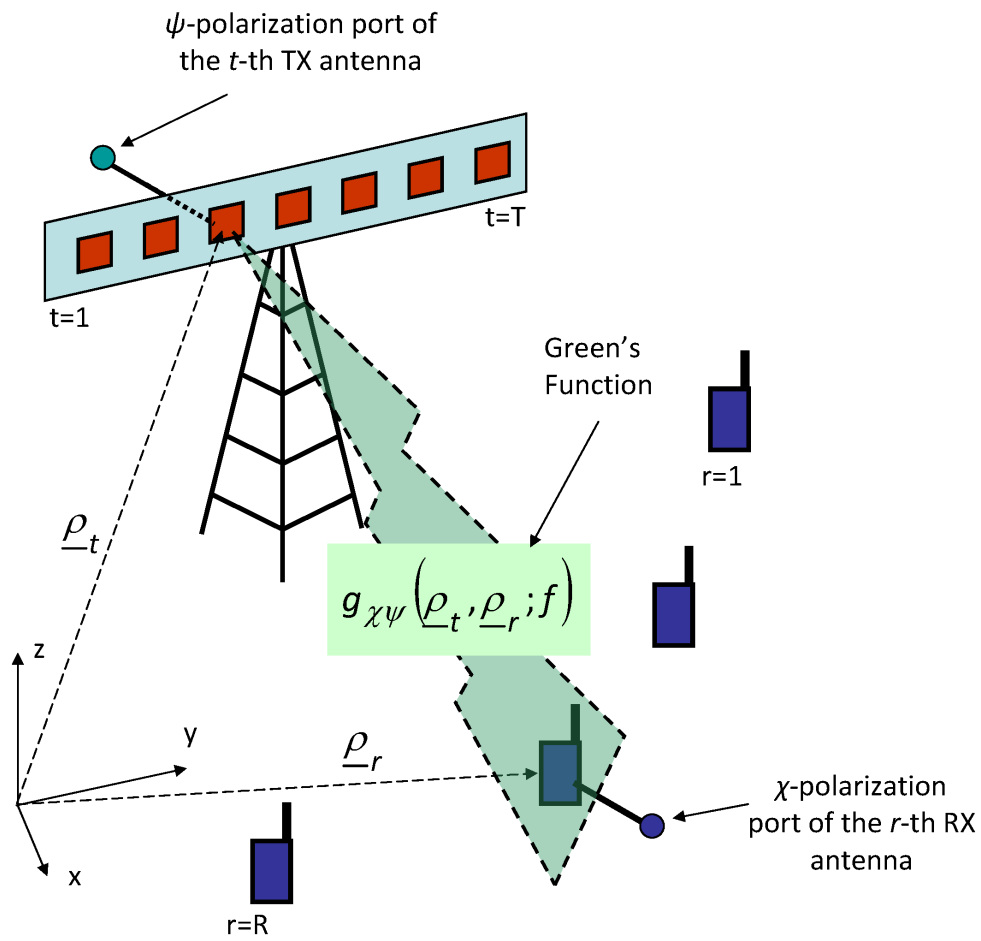
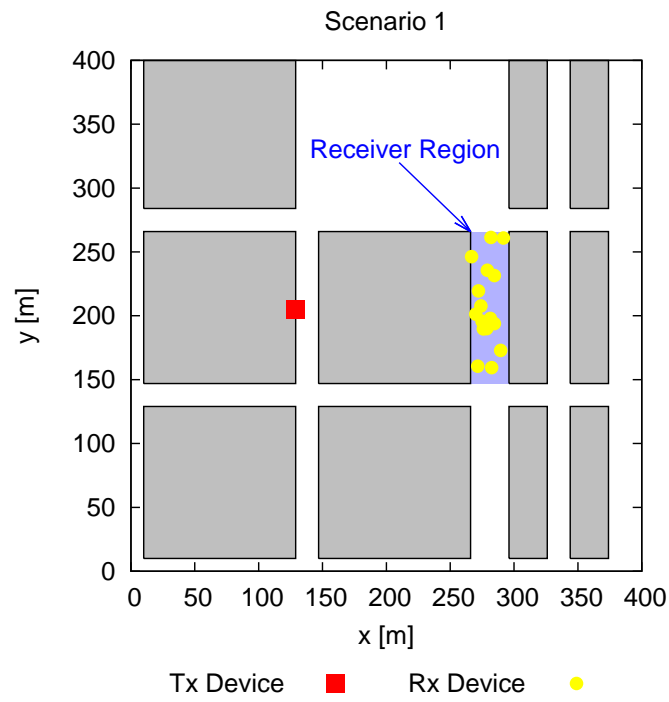
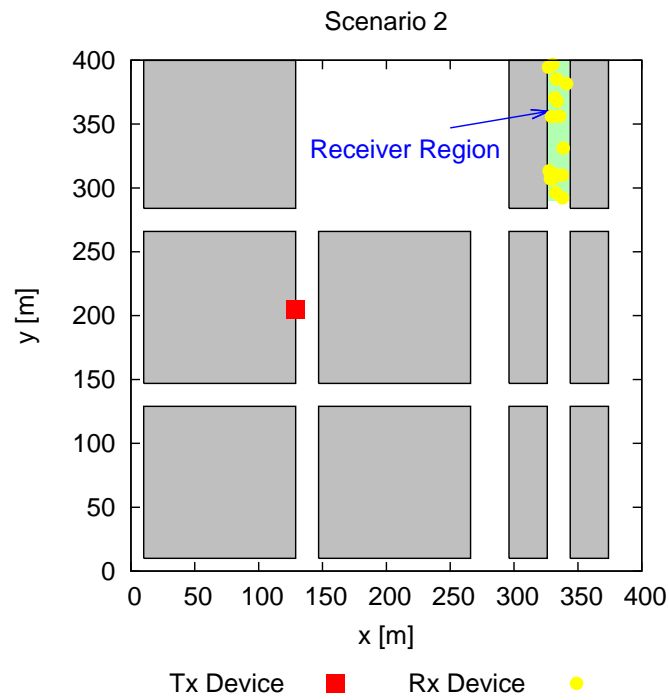


Figure 1 - G. Oliveri et al., "Capacity-Driven Low-Interference Fast Beam Synthesis ..."

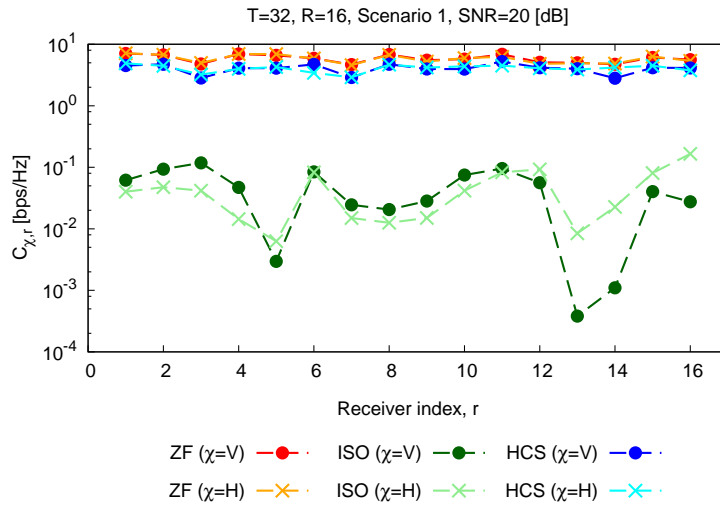


(a)

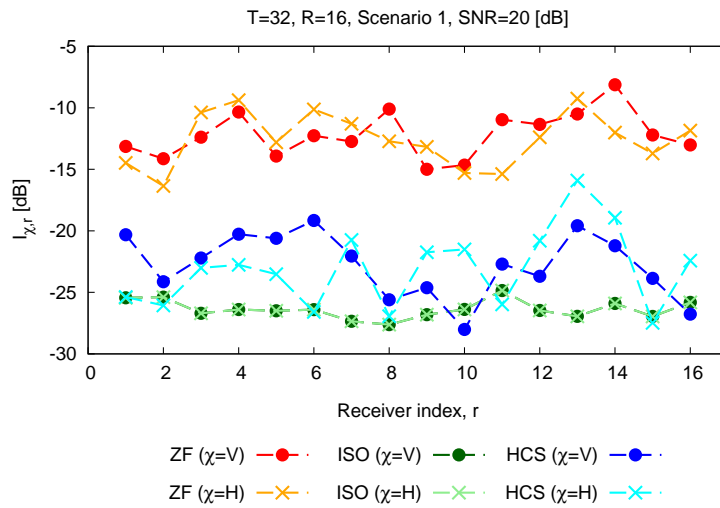


(b)

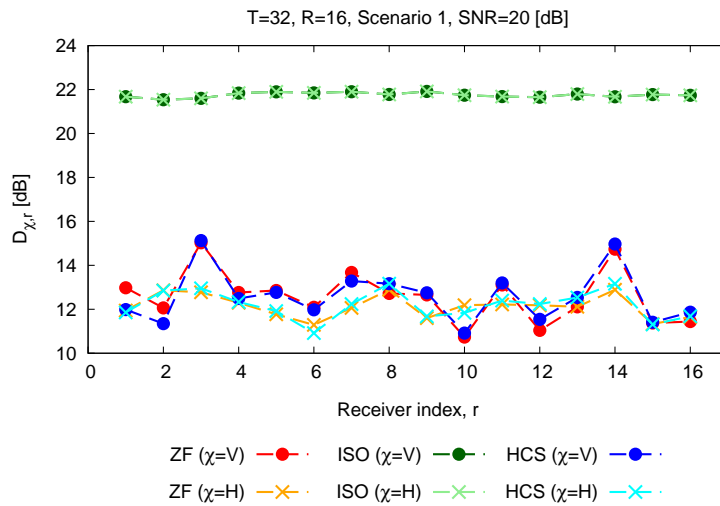
Figure 2 - G. Oliveri et al., “Capacity-Driven Low-Interference Fast Beam Synthesis ...”



(a)



(b)



(c)

Figure 3 - G. Oliveri et al., “Capacity-Driven Low-Interference Fast Beam Synthesis ...”

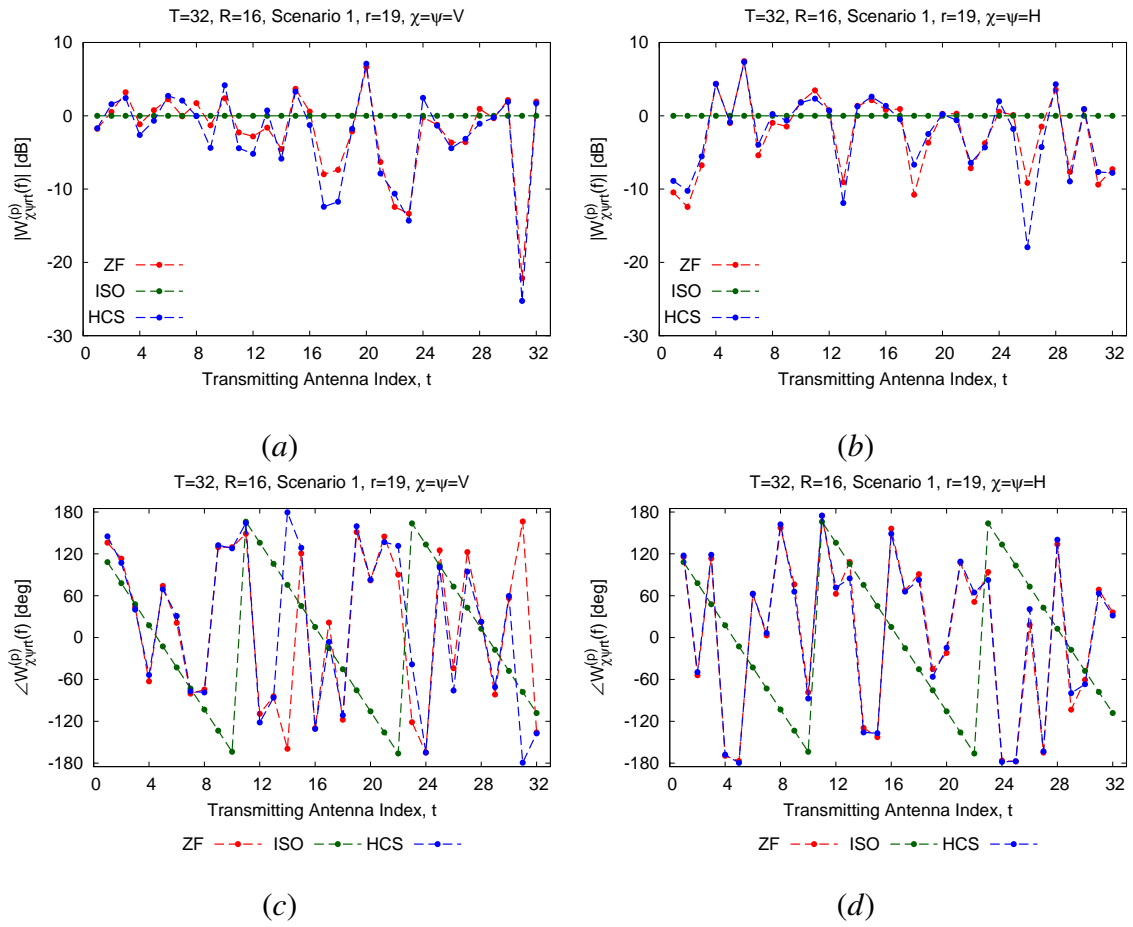
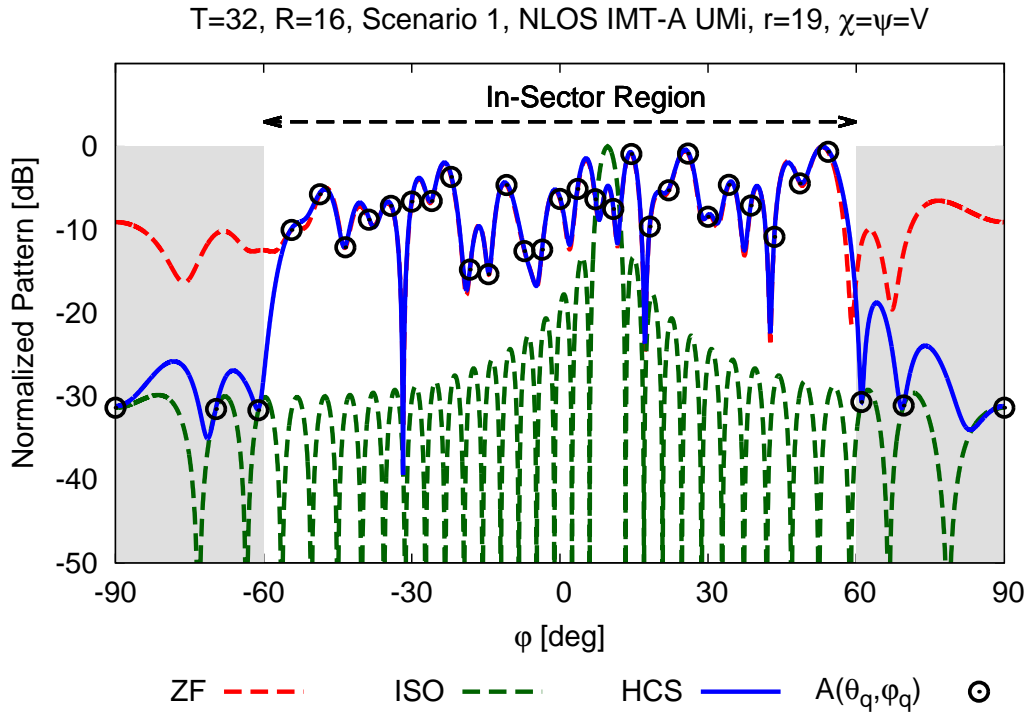
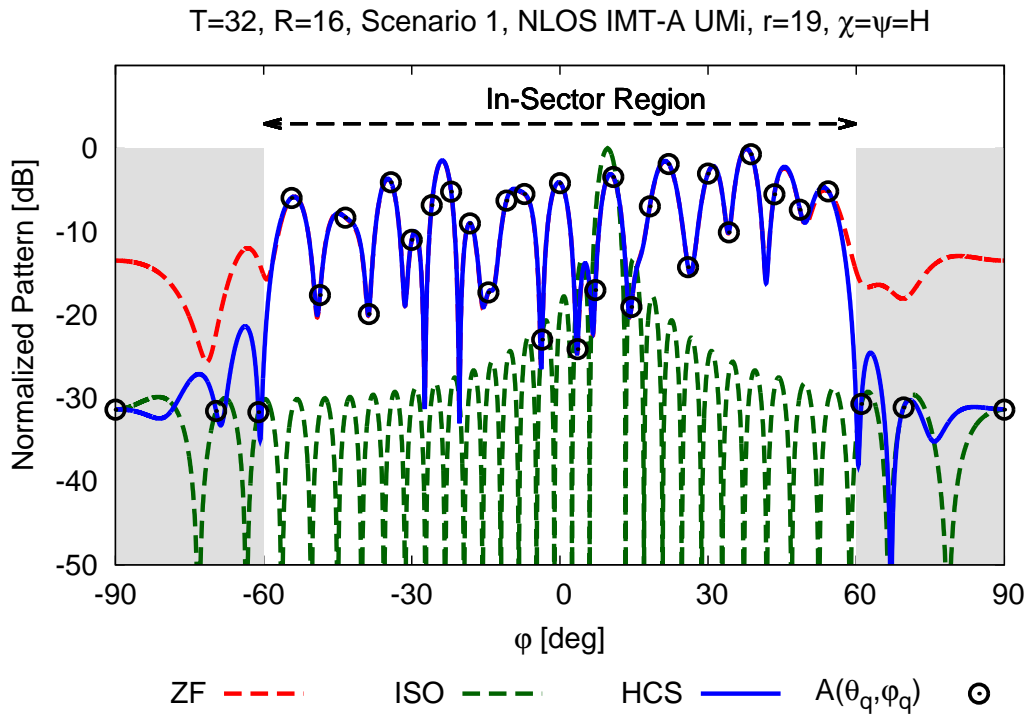


Figure 4 - G. Oliveri et al., “Capacity-Driven Low-Interference Fast Beam Synthesis ...”



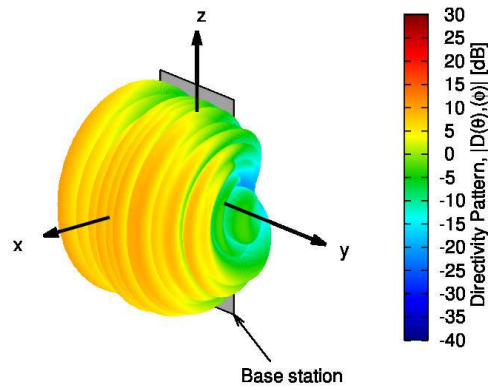
(a)



(b)

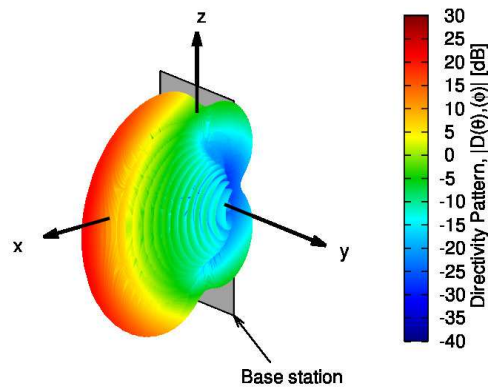
Figure 5 - G. Oliveri et al., “Capacity-Driven Low-Interference Fast Beam Synthesis ...”

NLOS IMT-A UMi, 'Bare CDM', S=32, L=16, Scenario 1, b=19



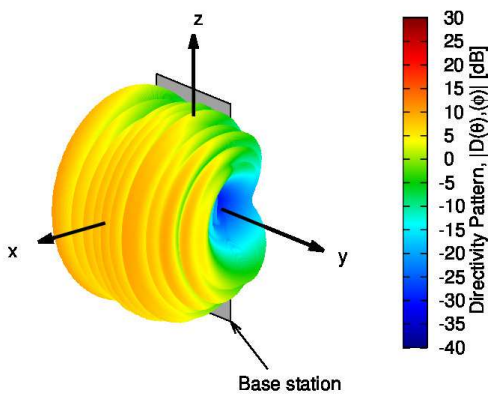
(a)

NLOS IMT-A UMi, 'Bare DDM', S=32, L=16, Scenario 1, b=19



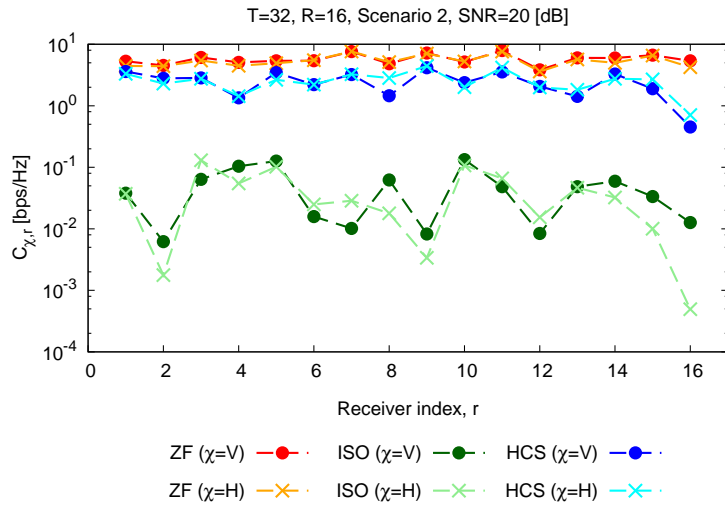
(b)

NLOS IMT-A UMi, 'SC-CDM', S=32, L=16, Scenario 1, b=19

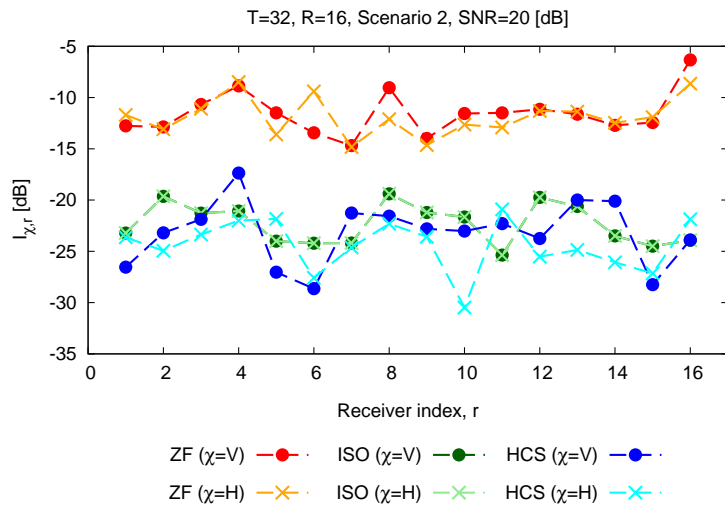


(c)

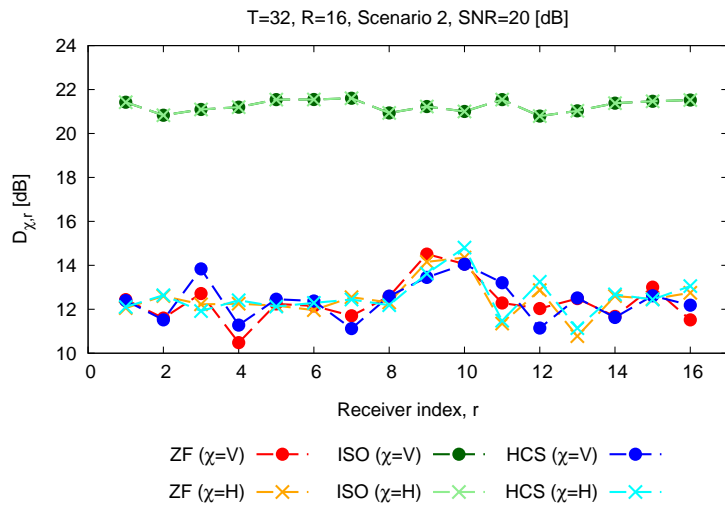
Figure 6 - G. Oliveri et al., "Capacity-Driven Low-Interference Fast Beam Synthesis ..."



(a)



(b)



(c)

Figure 7 - G. Oliveri et al., “Capacity-Driven Low-Interference Fast Beam Synthesis ...”

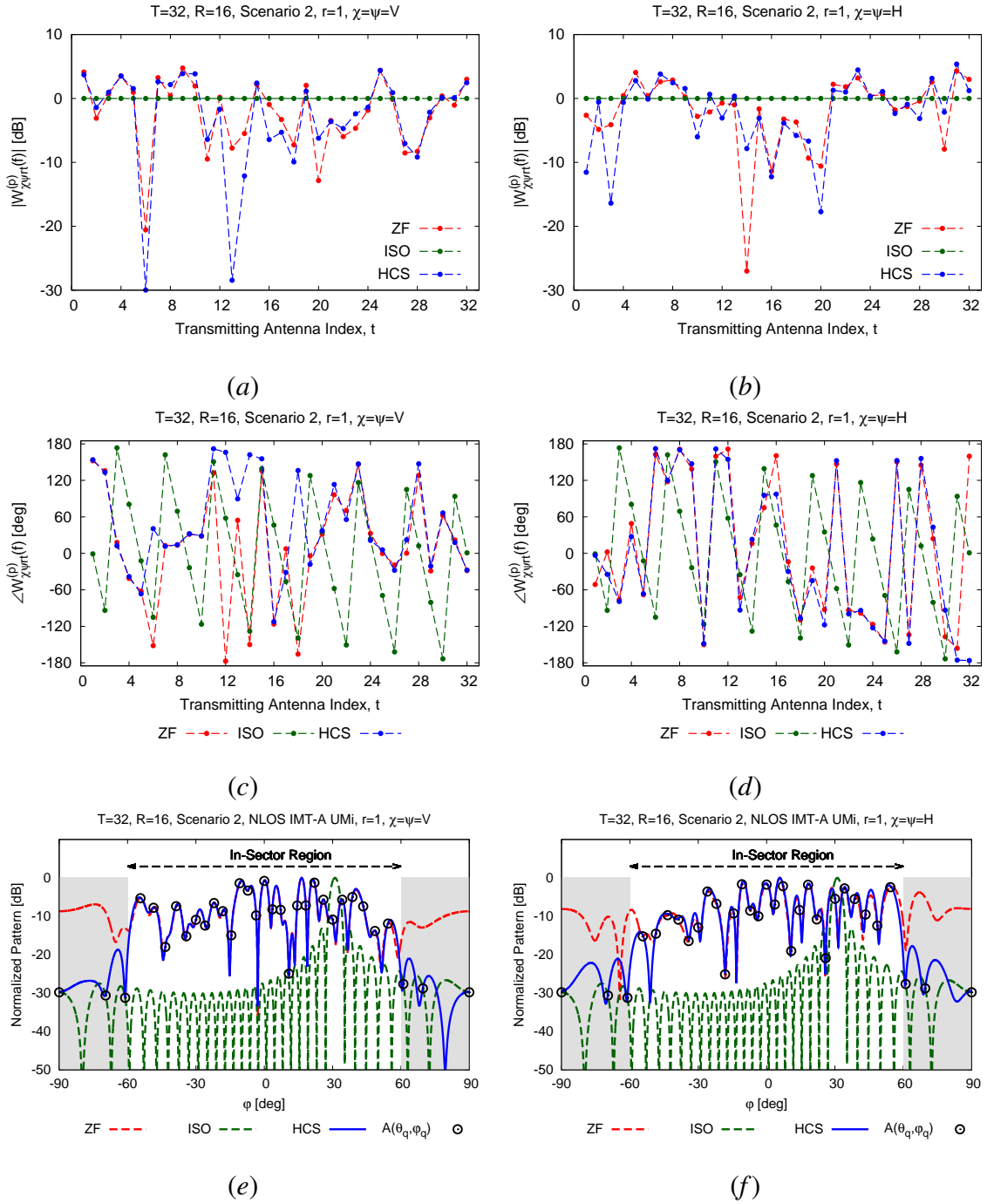
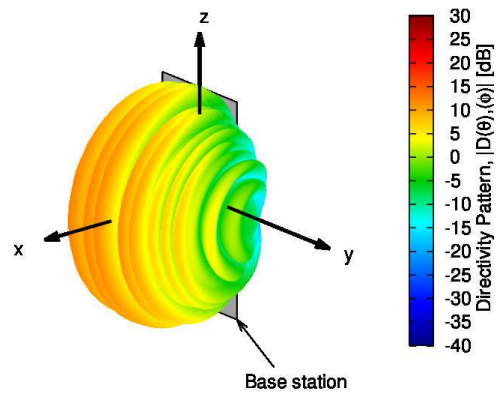


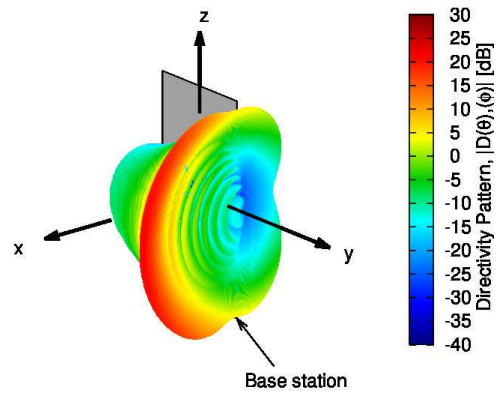
Figure 8 - G. Oliveri et al., “Capacity-Driven Low-Interference Fast Beam Synthesis ...”

NLOS IMT-A UMi, 'Bare CDM', S=32, L=16, Scenario 3, b=1



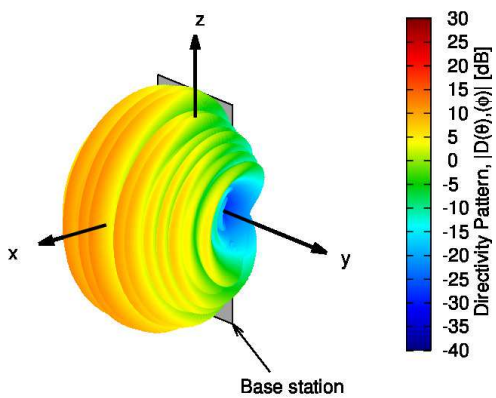
(a)

NLOS IMT-A UMi, 'Bare DDM', S=32, L=16, Scenario 3, b=1



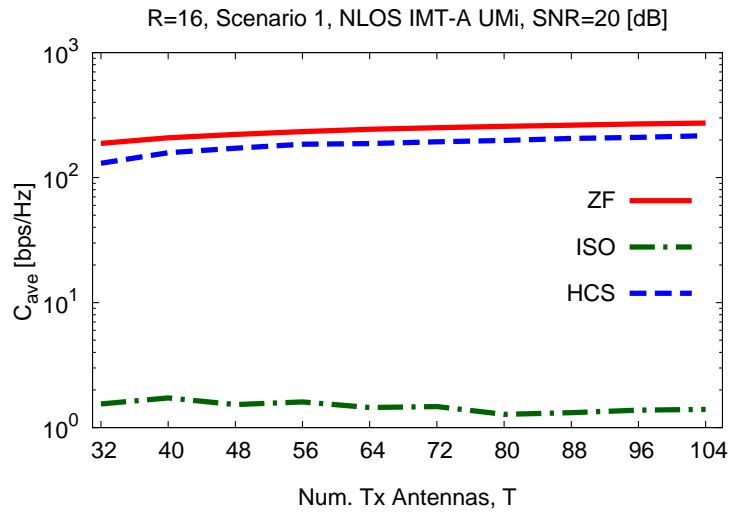
(b)

NLOS IMT-A UMi, 'SC-CDM', S=32, L=16, Scenario 3, b=1

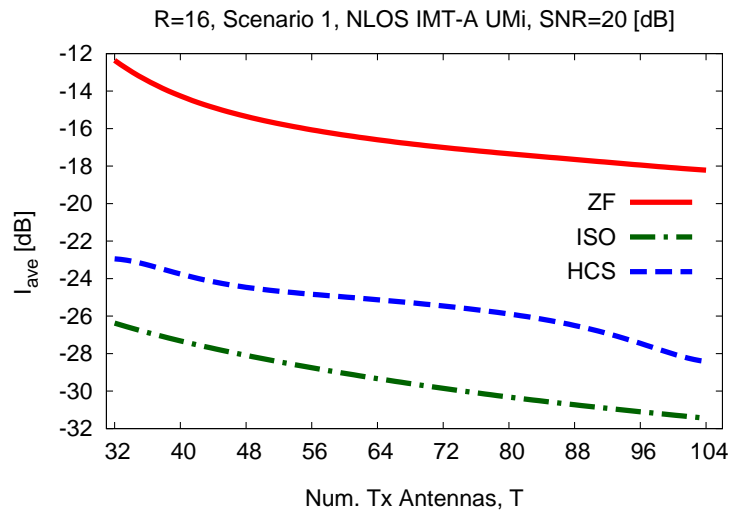


(c)

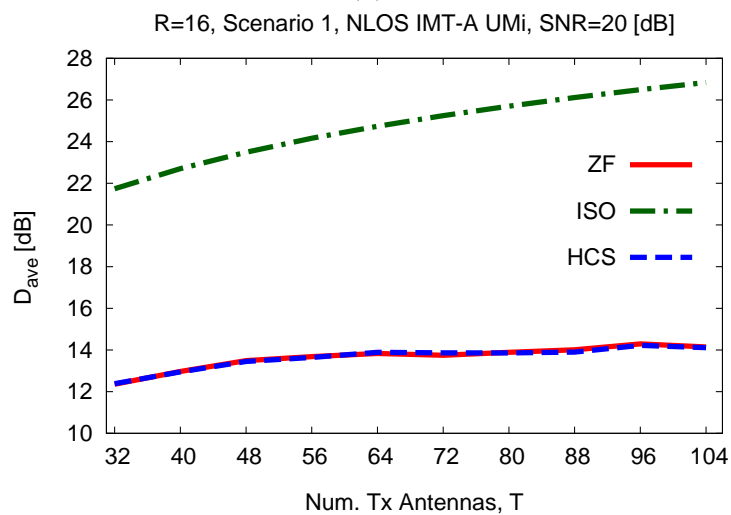
Figure 9 - G. Oliveri et al., "Capacity-Driven Low-Interference Fast Beam Synthesis ..."



(a)

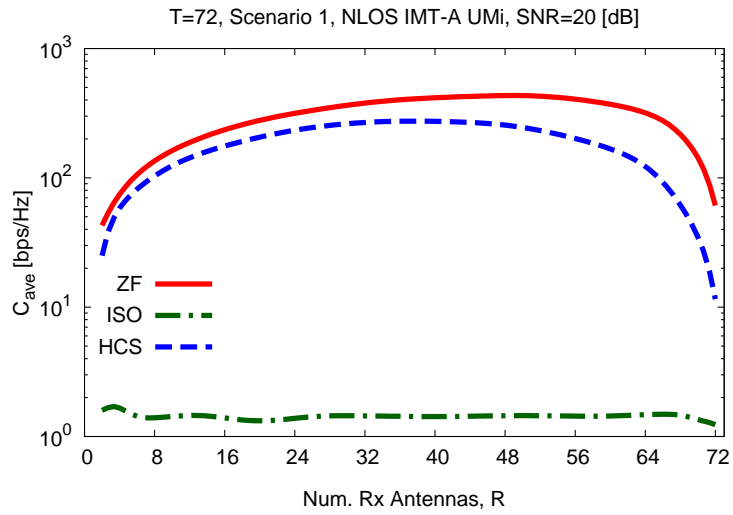


(b)

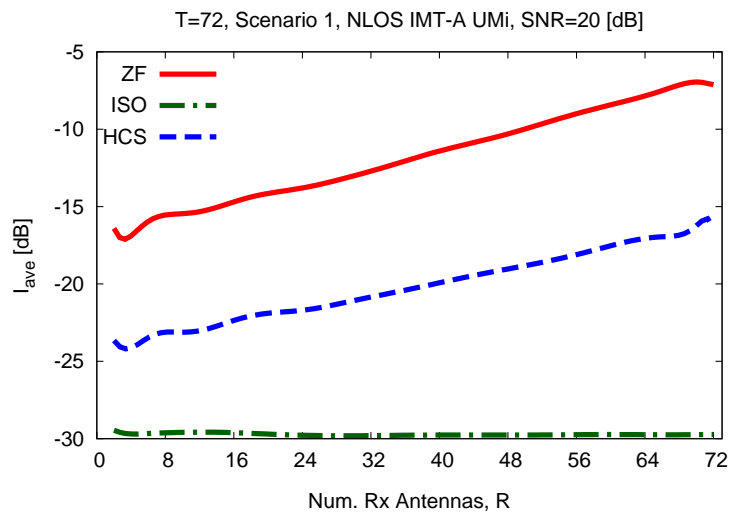


(c)

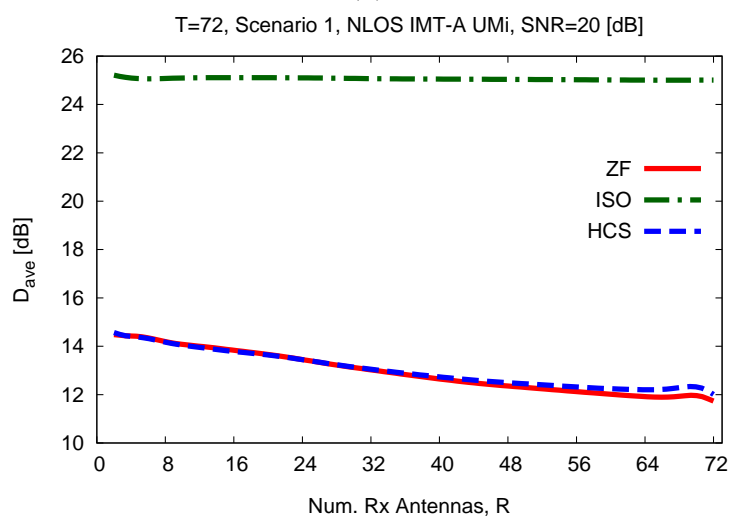
Figure 10 - G. Oliveri et al., "Capacity-Driven Low-Interference Fast Beam Synthesis ..."



(a)

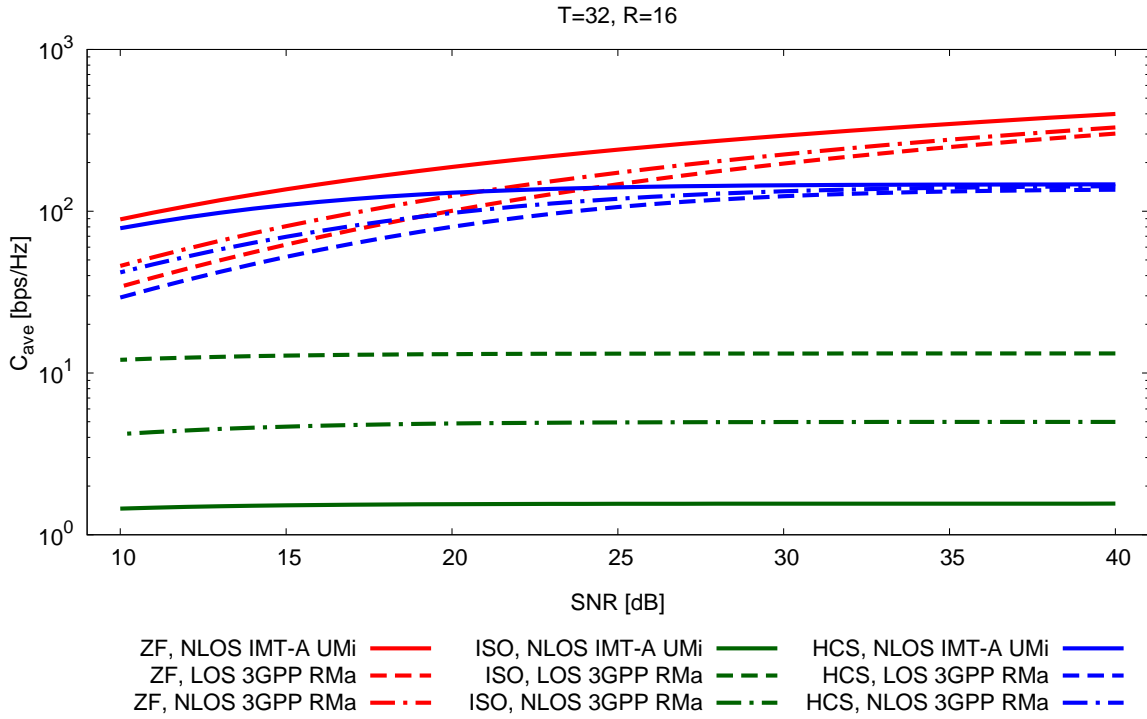


(b)

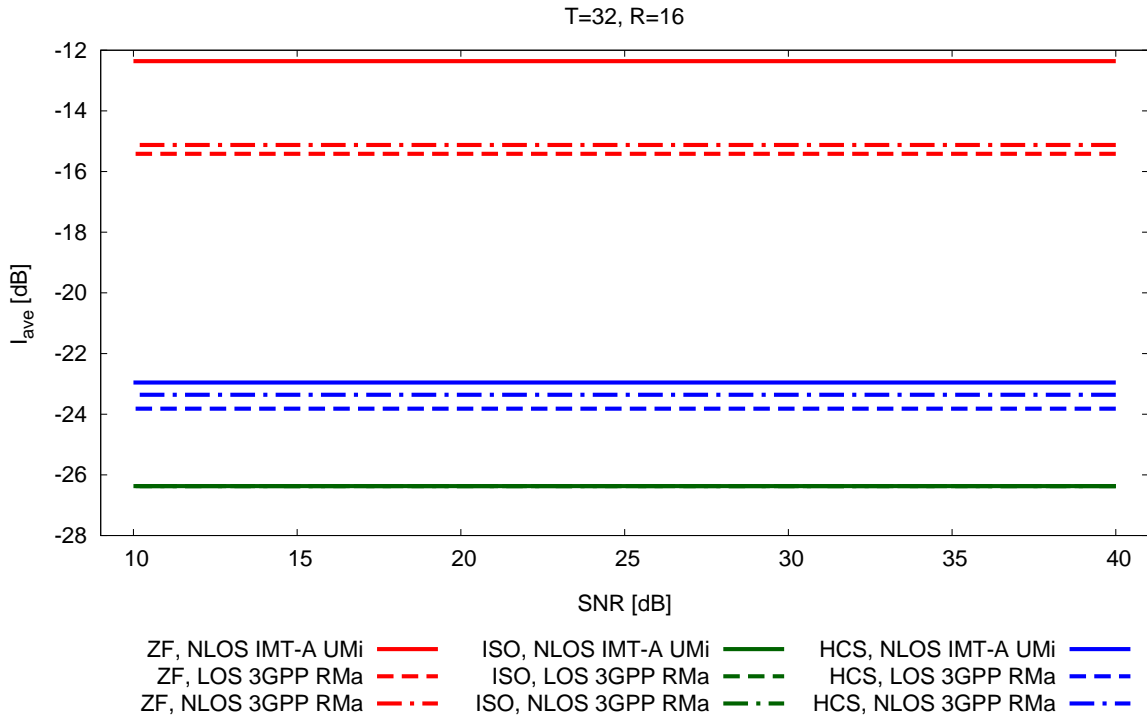


(c)

Figure 11 - G. Oliveri et al., "Capacity-Driven Low-Interference Fast Beam Synthesis ..."

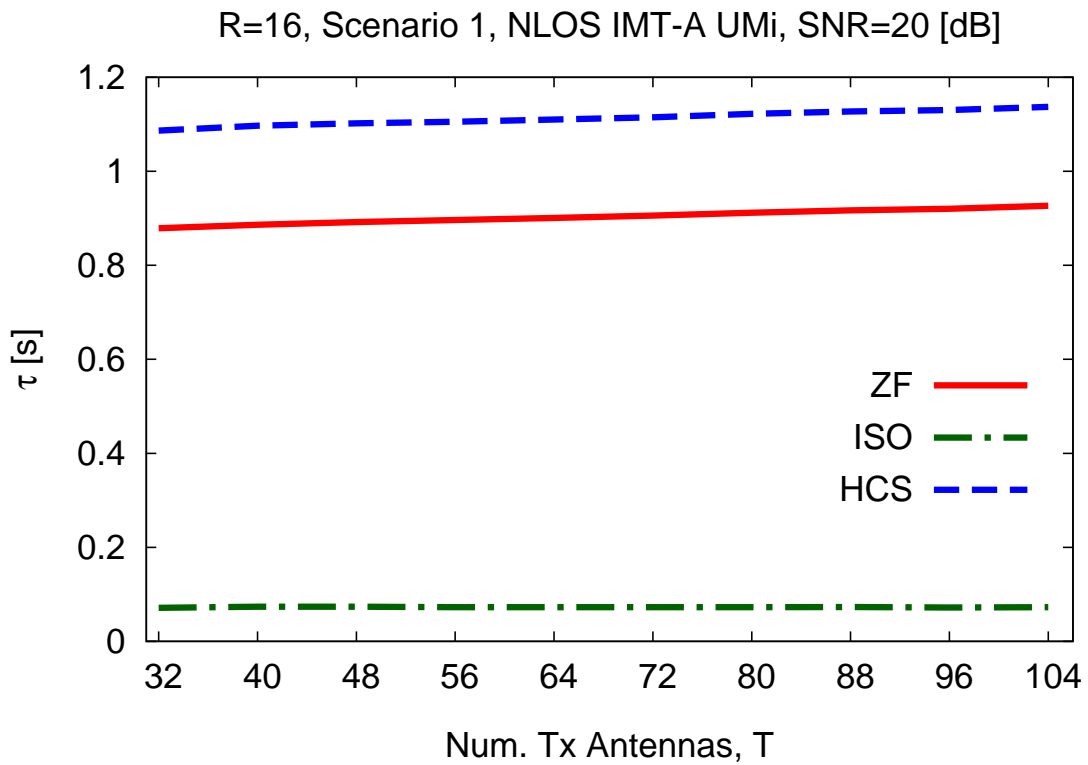


(a)

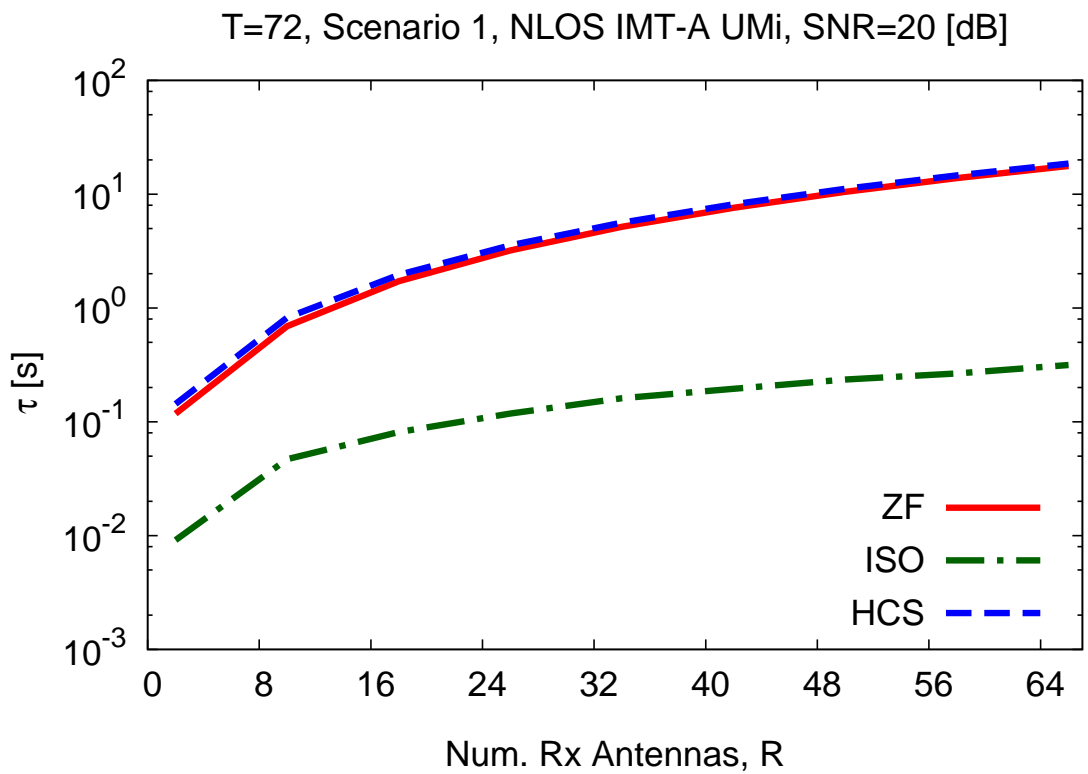


(b)

Figure 12 - G. Oliveri et al., “Capacity-Driven Low-Interference Fast Beam Synthesis ...”



(a)



(b)

Figure 13 - G. Oliveri et al., "Capacity-Driven Low-Interference Fast Beam Synthesis ..."

Approach	\mathcal{C}_{ave} [bps/Hz]	\mathcal{D}_{ave} [dB]	\mathcal{I}_{ave} [dB]
<i>ZF</i>	187.75	12.35	-12.36
<i>ISO</i>	1.55	21.74	-26.37
<i>HCS</i>	130.09	12.38	-22.95

Table I - G. Oliveri et al., "Capacity-Driven Low-Interference Fast Beam Synthesis ...

Approach	\mathcal{C}_{ave} [bps/Hz]	\mathcal{D}_{ave} [dB]	\mathcal{I}_{ave} [dB]
<i>ZF</i>	179.16	12.40	-11.73
<i>ISO</i>	1.46	21.26	-22.34
<i>HCS</i>	81.37	13.05	-21.82

Table II - G. Oliveri et al., “Capacity-Driven Low-Interference Fast Beam Synthesis ...